Stony Brook University

Thermal Emission Spectral Characterization of Sandstones and Mudstones

A Thesis Presented

by

Michael Terrance Thorpe

to

The Graduate School

in Partial Fulfillment of the

Requirements

for the Degree of

Master of Science

in

Geoscience

Stony Brook University

December 2014

Stony Brook University

The Graduate School

Michael Terrance Thorpe

We, the thesis committee for the above candidate for the

Master of Science degree, hereby recommend

acceptance of this thesis.

A. Deanne Rogers– Thesis Advisor
Assistant Professor of Geosciences

Timothy Glotch– Second Reader
Associate Professor of Geosciences

Scott McLennan-Third Reader
Professor of Geosciences

This thesis is accepted by the Graduate School

Charles Taber
Dean of the Graduate School

Abstract of the Thesis

Thermal Emission Spectral Characterization of Sandstones and Mudstones

by

Michael Terrance Thorpe

Master of Science

in

Geosciences

Stony Brook University

2014

Thermal emission spectroscopy was used to determine the mineralogy of sandstone and mudstone rocks as part of an investigation of linear spectral mixing between sedimentary constituent phases. With widespread occurrences of sedimentary surfaces on Mars, the critical examination of sedimentary rocks spectral behavior provides a basis for interpreting the environment controlling the mineralogical history of this planet. Unmixing algorithms for thermal infrared rock spectra have previously proven to be a viable technique, with accuracies better than ~17 vol %. However, sedimentary rocks, with natural variation of composition, compaction, and grain size, have yet to be critically examined. In this work, we present an analysis of the thermal emission spectral (~270-1650 cm^{-1}) characteristics of a suite of 12 sandstones and 15 mudstones, establishing a foundation for remote spectral studies of sedimentary surfaces. Results from this work are consistent with previous thermal emission spectroscopy studies and indicate that bulk rock mineral abundances can be estimated within 10 vol % for sandstones and within 20 vol % for mudstones, in comparison to traditionally used

mineralogical techniques. During this investigation, X-ray diffraction, microRaman spectroscopy, and traditional point counting procedures were all evaluated in comparison with thermal emission spectroscopy and it was determined that each method contains its own intrinsic limitations. With thermal emission spectroscopy at the focal point of this work, it is concluded that derived mineralogy from spectral unmixing is an advantageous technique for mineral clasts; however, this technique remains highly ambiguous for the matrix (< 30 μm) fraction of sedimentary rocks.

Dedication Page

I would like to dedicate this thesis to my three grandmothers that began this journey with me and have unfortunately passed away during its duration. Grandma Sooky, Grandma Rosie, and Mama Done, you have always encouraged and inspired me to reach new heights. Thank you for your words of wisdom and thank you for watching over me.

Table of Contents

List of Figures

List of Tables

List of Abbreviations

TIR- thermal infrared

MER- Mars Exploration Rover

MSL- Mars Science Laboratory

XRD (QXRD)- X-ray diffraction (quantitative)

IR- infrared

FTIR- Fourier transform infrared

RMS- root mean square

Acknowledgments

I would like to acknowledge and thank my advisor, Deanne Rogers, for all her guidance and encouragement in completing this thesis. Also, I would like to extend my gratitude to my committee members, Timothy Glotch and Scott McLennan, for their helpful advice during this process as well as the useful remarks provided towards this thesis. A special thanks is also given to Scott McLennan for donating samples to this project.

Furthermore, I would like to thank Thomas Bristow, from the NASA Ames Research Center, for undertaking the X-ray diffraction portion of this investigation. I would also like to recognize my fellow graduate student, Steven Jaret, and thank him for the help provided on various parts of this project.

Lastly, I would like to extend more than thanks to my family and girlfriend, Danielle. Love and support keeps the mind at ease, and for that I appreciate you encouragement throughout the duration of this thesis.

1. Introduction

On Earth, compositional studies of sedimentary rocks provide a framework for understanding how tectonic, climatic, and biogeochemical processes have evolved over Earth's history [*McLennan et al*., 1993]. The composition of sedimentary rocks has been used as a proxy to decipher Earth's geologic evolution and include (but not limited to) such techniques as: the use of grain sorting and matrix present to deduce the fluid conditions during deposition [*Pettijohn, F.J*., 1954], the calculation of feldspar and clay ratios to determine the extent of chemical weathering in sandstones and mudstones [*Nesbitt and Young*, 1996], and the measurement of neodymium isotopes from sandstones and siltstones to identify the age of provenance material [*McDaniel et al*. 1994]. However, the sedimentary rock record on Earth is limited to only the latter part of Earth's history, due to a variety of plate tectonic processes. The same type of tectonic activity that has demolished the sedimentary rock record on Earth preceding the Archean (4.0 Gyr), appears to be absent from the surface of Mars, and thus a more extensive geologic timescale is preserved in the Martian sedimentary rocks [*McLennan*, 2012].

Early exploration of Martian terrain resulted in a perception of a lunar-like landscape, dominated by volcanic and impact processes [e.g., *Kieffer et al.,* 1992]. With increasing spatial resolving power of subsequent imagers, beginning with Mars Global Surveyor, finely layered outcrops were discovered, suggesting a sedimentary history and possibly aqueous activity [*Malin and Edgett*, 2000]. Similarly, from global compositional mapping using infrared spectrometers, the surface of Mars is clearly dominated by basaltic compositions [*Bandfield et al.*, 2000]. With the advent of spectrometers with higher spatial resolution, hundreds of outcrops of sulfate-, carbonate-, and phyllosilicate-bearing rocks have been discovered, revealing a dynamic sedimentary history on Mars [*Bibring et al*., 2006;*Murchie et al*., 2009; *Ehlmann et al*., 2011].

The *Sprit*, *Opportunity*, and *Curiosity* rovers have each encountered sedimentary rocks along their traverses. The Mars Exploration Rover (MER), *Opportunity,* identified sulfate-rich, cross-bedded sandstones that contain hematite spherules at Meridiani Planum [*Squyres et al.*, 2004]. Based on the detailed mineralogy and sedimentary facies observed, the rocks were interpreted as evaporites that have been reworked and mixed with basaltic clastic material, transported and lithified by evaporitic cements in a dune/interdune environment. The spherules were interpreted to have formed through diagenetic fluids that remobilized iron within the evaporitic sandstone unit; subsequent erosion of the unit preferentially left a lag deposit of the more erosion-resistant spherules.

At Gusev Crater on Mars, there is a lack of extensive sedimentary units, however, some sulfate and carbonated-cemented rocks were encountered as loose float in the Columbia Hills. The instruments aboard the Mars Exploration Rover, *Spirit,* returned geological, geochemical, and mineralogical data from the Columbia Hills indicative of alteration products from an aqueous episode on the surface of Mars [*Squyres et al.*, 2006]. The "Peace Class" rocks of Columbia Hills have been interpreted as basaltic sandstones formed from the saturation of ultramafic sand with a sulfate rich fluid and eventual evaporation [*Squyres et al.*, 2006]. Furthermore, MER *Spirit* returned Miniature Thermal Emission Spectrometer data that indicated Mg-Fe rich carbonates present in the Comanche outcrops in Columbia Hills [*Morris et al*., 2010]. These outcrops represent a diverse aqueous history that altered only the top portion of an olivine-rich volcaniclastic Algonquin class, leaving behind a stratigraphy of a heavily altered and carbonate enriched upper unit, an unaltered lower unit, and an intermediate middle unit [*Ruff*, 2014].

The Mars Science Laboratory (MSL) *Curiosity* rover has encountered a succession of sedimentary rocks during its traverse at the landing site of Gale Crater. Yellowknife Bay has a rich sedimentary history that has been characterized in terms of mineralogy [*Vaniman et al*., 2014], geochemistry [*McLennan et al*., 2014], and stratigraphy [*Grotzinger et al*., 2014]. The primary composition of the two mudstones sampled, John Klein and Cumberland, consists of detrital basaltic minerals, iron oxides and sulfides, calcium sulfates, smectites, and a substantial amorphous component [*Vaniman et al*., 2014]. The data returned from Yellowknife Bay has led to a self-consistent interpretation of an ancient fluvial-lacustrine environment constrained by at least two distinct diagenetic episodes [*McLennan et al*., 2014].

Given that the mineralogy is a key aspect in understanding chemical and physical conditions of sedimentary transport, deposition, and provenance, the expansion of remote sensing capability in determining rock composition becomes critically important. One of the techniques that is routinely used to estimate rock compositions remotely is thermal emission spectroscopy; however, most laboratory studies used to validate the accuracy of mineral abundance derived from thermal emission spectra have been focused on coarse grained igneous rocks and sands [*Feely and Christensen*, 1999; *Wyatt et al*., 2001; *Michalski et al*., 2004]. The spectral behavior of loose particulate (e.g. unpacked) fine-grained samples results in non-linear spectral mixing due to the volume scattering that occurs due to the grain size being relatively small in respect to the wavelength of mid-IR light (2.5-50μm), which in turn produces inaccurate mineral abundance determinations [*Ramsey and Christensen*, 1998]. However, the spectral mixing behavior of naturally compacted fine-grained materials, such as those associated with sedimentary deposition, has not been characterized in detail. Synthetic mixtures composed of packed fine-grained materials exhibit minimal volume scattering [*Salisbury and Walter*, 1989];

thus one might expect that naturally compacted sediments and cemented mudstones and sandstones may show similar behavior.

The goal of this thesis is to therefore, assess the capability of thermal emission spectroscopy to determining the mineralogy of sandstones and mudstones in order to enhance our interpretations of the Martian surface. This will be accomplished by conducting a cross analysis of petrographic images, X-Ray diffraction (XRD) patterns, and microRaman spectra in comparison with the mineral abundances derived from the bulk rock thermal emission (TIR) spectra of a suite of terrestrial sandstones and mudstones.

A literature review of relevant TIR and microRaman studies is presented in Section 2, to display the utility of thermal emission spectroscopy in investigating a variety of geological materials, but also to emphasize the knowledge gap that exists in the characteristics of sedimentary rocks within the TIR. Section 3 of this thesis includes a detailed description of the methodology and analytical techniques. Section 4 presents the results of this work, followed by our interpretations in Section 5. In section 6, I include recommendations for data reduction, and evaluation of the utility of TIR measurements in future Mars missions.

2. Background

2.1 Thermal Emission Spectroscopy

Thermal emission spectroscopy, a form of vibrational spectroscopy, is sensitive to molecular bending and stretching vibrational modes present in any material. The frequencies of vibration (~100-10000 cm^{-1}, or ~1-100 μm) are related to the chemical composition and structure of the mineral. Thermal emission spectroscopy is useful for geologic remote sensing applications because individual minerals have unique and characteristic molecular vibrational bands [*Thomson and Salisbury*, 1993]. Thermal emission spectrometers aboard orbital and rover missions have returned data that have greatly increased our perception of the aqueous history of

the Martian surface, including identification of large areas containing crystalline hematite [*Christensen et al.*, 2001; *Glotch and Christensen*, 2005; *Glotch and Rogers*, 2007] (later investigated by the *Opportunity* rover), deposits of amorphous silica and sulfate [*Bandfield*, 2008; *Glotch et al*., 2006; *Ruff et al*., 2007], and carbonate-bearing basalts [*Ruff et al*., 2014]. Laboratory work was the predecessor to these orbital interpretations; and the framework of mineral quantification from emission spectra was established by several studies.

2.2 Previous thermal emission studies on rocks

Using the laboratory thermal emission measurement techniques described by *Ruff et al.,* [1997], thermal emission spectral libraries of many common rock-forming minerals were developed [*Christensen et al.*, 2000]. These libraries were then used to test the validity of mineral mixing in multi-component samples. *Ramsey and Christensen,* [1998] used a deconvolution and linear retrieval algorithm to investigate the spectral behavior of minerals in a mixture. Using a chi-square minimization technique, they were able to model and accurately identify up to 15 minerals in a mixture of sand-sized particles or larger, to accuracies within 5% on average [*Ramsey and Christensen*, 1998], demonstrating that components in a sample spectrum contribute to the overall spectrum in proportion to their areal abundance.

Feely and Christensen, [1999] investigated the thermal emission spectral mixing behavior of 45 igneous and 51 metamorphic rocks, in which they concluded that the derived mineral abundances for primary minerals (feldspars, quartz, pyroxene, and carbonates) agreed within 7-15% of the optically determined abundances. Subsequently, *Hamilton and Christensen*, [2000] obtained similar results for 20 mafic and ultra mafic rocks by recovering modal mineralogy within 5-15% for 92% of their samples; and investigation of 28 terrestrial basalts and

andesites returned absolute differences ranging from 2.4-12.2 vol % [*Wyatt et al.*, 2001]. *Michalski et al*., [2004] studied 46 weathered granitic rocks that resulted in mineral abundances within 0-15% of the petrologically determined modes. However, not all rocks demonstrate linear mixing behavior. From examination of TIR spectra of evaporites, *Baldridge et al*., [2004] concluded that samples containing a significant amount of halite, or possible fine-grained material, result in an unsatisfactory model due to transparency of these materials in the TIR and thus increased volume scattering effect. Similar results were determined from the analysis of 22 clay-bearing mudstones, where *Michalski et al*., [2006] determined that linear unmixing of TIR spectra can provide adequate clay abundance estimates (within ~4%) but the identification of individual clay mineral phase abundances is insufficient within an intimate mixture.

These studies established a foundation for the interpretation of orbital and rover data, but there still remains a knowledge gap in the spectral characterization of sedimentary rocks. In particular, mudstones (grain sizes < 62.5μm) of a varying composition from previously analyzed mudstones as well as sandstones (62.5μm > grain size < 2 mm) consisting of larger clasts mixed with an intimate matrix component. With the identification of mudstones at Yellowknife Bay [*McLennan et al*., 2014] and sandstones at Gusev Crater [*Squyres et al.*, 2006], the opportunity to enhance the understanding of sedimentary rock thermal emission features becomes critical to future Mars research.

2.3 Current methods for determination of sedimentary rock mineral abundances

Traditional Petrologic analysis

The petrologic analysis of sedimentary rocks, which consists of systematically scanning thin sections and optically identifying individual detrital grains, is one of the more traditional

techniques in quantification of mineralogy. The reliability associated with this technique is dependent on the amount of points counted, with typical accuracies of ±5-15% for major modes [*Van der Plas and Tobi*, 1965]. This method has been commonly used to classify sedimentary rocks and determine their provenance by separating mineral phases into distinct modes based on texture and optical properties [*Pettijohn,* 1975]. However, this method is limited to identification of sand-sized or larger grains (>~62.5 μm). Traditionally, the mineral phases present in the grain size fraction below this limit are grouped together and qualitatively assessed.

X-Ray Diffraction

Powder X-ray diffraction pattern analysis of sedimentary rocks has become routine for quantifying mineral abundances. Techniques and sample preparation particularly designed to quantify individual clay phases (that are subject to orientation effects) have been developed [*Moore and Reynolds Jr*, 1997] and have proven to provide accuracies within 2 wt% of the accepted value [*Środon et al*., 2001]. The more extensive care in preparing the samples for analysis by XRD has in turn provided a more quantitative analysis of the fine-grained matrix fraction of a sample in comparison to the traditional petrologic analysis, which can only qualitatively assess this component. Quantitative XRD (QXRD) procedures have been employed in numerous studies and include (but are not limited to) the investigation of mineralogy in order to determine provenance of sandstones from eastern Australia [*Ward et al.*, 1999], the examination of clay mineralogy in organic rich shales from Cambrian sedimentary basins [*Tosca et al.*, 2010], and more recently, the interpretation of data returned from the *Curiosity* rover at Yellowknife Bay, Gale Crater, Mars to discover that the mineralogy and geochemistry of rock samples are consistent with a mudstone composition [*Vaniman* et al., 2014].

MicroRaman Spectroscopy

The strategy of utilizing microRaman spectroscopy for an alternative point counting procedure has been used in previous studies and was most notably developed by *Haskin et al.*, [1997]. The use of this technique has been proven to be reasonably consistent with the traditional point counting procedures and allows for an unambigous identification of minerals [*Wang et al.*, 1999]. Raman spectroscopy is an appealing technique for fine-grained samples because the peaks associated with each mineral phase shift are stong, distinct, and confined to that particular phase; therefore allowing the distinct identification of mineral phases that can not be determined by tradtional point counting procedures [*Z Ling et al.*, 2011a]. This method has been used to identify the mineral modes of highly weathered basalts but was limited in the accuracy of quantifying abundances [*Wang et al.*, 1999]. Ensuing work investigated the mineralogy and geochemistry of lunar soils, in which results were determined to be consistent with electron-microprobe and X-ray imaging methods [*Z C Ling et al.*, 2011b]. MicroRaman spectroscopy was also selected for comparison in this study because a cross analysis between two remote sensing techniques will provide a valuable insight for future data returned from rover and orbital missions.

3. Methods

3.1 Sample Description and Preparation

I examined 12 sandstones (modal grain size > 100 μm) and 15 mudstones (modal grain size < 100 μm) (**Table 1**) using multiple analytical techniques. The use of natural samples allowed for a wide range of compositions and grain sizes, as well as naturally occurring compaction and porosity to be examined.

Sandstones were acquired from the Stony Brook University Geosciences Department's Sedimentary Rock Collection. Mudstone samples from the Huronian Supergroup (2.5-2.2 Ga) outcrop belt on the northern shore of Lake Huron, Canada were donated by Scott McLennan.

Sample Name	Formation	Sample Source Description	Rock Type	Modal Clasts Grain Size (µm)	Sample Description
La Boca	La Boca	Stony Brook University Sedimentary collections	Sandstone	300	Tan to brown sandstone with rounded to sub-angular and moderately sorted grains
Tx-Te-1	-	Stony Brook University Sedimentary collections	Sandstone	300	Gray sandstone with rounded to sub-angular and poorly sorted grains
16-606	-	Stony Brook University Sedimentary collections	Sandstone	100	Gray sandstone with sub-rounded to well rounded and well sorted grains
Catskill SK-1	Catskill	Stony Brook University Sedimentary collections	Sandstone	300	Dark gray sandstone with sub-angular to sub-rounded and poorly sorted grains
DI-72-91	-	Stony Brook University Sedimentary collections	Sandstone	200-400	Gray sandstone with sub-rounded and well sorted grains
Devil K	-	Stony Brook University Sedimentary collections	Sandstone	200	Tan sandstone with round and well sorted grains
Smithwick	Smithwick	Stony Brook University Sedimentary collections	Turbidtic sandstone	300	Gray sandstone with sub-angular to sub-rounded and well sorted grains
Mis-Te-2	-	Stony Brook University Sedimentary collections	Sandstone	250	Red sandstone with sub-angular and well sorted grains
Flatirons	Fountain	Personal collections. Flat Irons Boulder, CO	Sandstone	400-700	Red sandstone with sub-angular and poorly sorted grains
Berea	Berea	Wards Sedimentary Collection #45. Berea, Ohio.	Sandstone	200-300	Gray sandstone with angular to sub-angular and moderately sorted grains
Gratton	Gratton	Wards Sedimentary Collection #51. Gratton, NY.	Sandstone	100-400	Graywacke with angular to sub-angular and poorly sorted grains
Mt. Tom	Sugarloaf	Wards Sedimentary Collection #50. Mt. Tom, MA.	Sandstone	500	Arkoses with sub-angular and poorly sorted grains

SM-75-142	McKim	Scott McLennan's collections. Huronian sequence	Claystone	1.95-4	Gray clayey shale with silt laminae
SM-75-120	McKim	Scott McLennan's collections. Huronian sequence	Mudstone	1.95-62.8	Gray mudstone
SM-75-117	Pecors	Scott McLennan's collections. Huronian sequence	Sandy clayey siltstone	1.95-4	Gray clayey shale with silt-very fine sand laminae
SM-75-107	Gowganda	Scott McLennan's collections. Huronian sequence	Clayey mudstone	1.95-4	Gray clayey laminated mudstone
SM-75-104	Gowganda	Scott McLennan's collections. Huronian sequence	Mudstone	1.95-62.8	Gray clayey laminated mudstone
SM-75-134	Gowganda	Scott McLennan's collections. Huronian sequence	Siltstone	4-62.8	Gray silty mudstone
SM-75-152	Espanola	Scott McLennan's collections. Huronian sequence	Silty dolostone	4-62.12	Dolomite with dark gray silt laminae
SM-75-161	Espanola	Scott McLennan's collections. Huronian sequence	Silty limestone	4-62.8	Limestone with dark gray silt laminae
SM-75-158	Gordon Lake	Scott McLennan's collections. Huronian sequence	Silty mudstone	4-62.8	Gray silty laminated mudstone
SM-75-167	Gowganda	Scott McLennan's collections. Huronian sequence	Mixite	4-62.8	Dark gray mudstone
SM-75-113	McKim	Scott McLennan's collections. Huronian sequence	Mudstone	1.95-62.8	Gray mudstone
SM-75-105	Gowganda	Scott McLennan's collections. Huronian sequence	Mudstone	1.95-62.8	Gray clayey shale with silt laminae
SM-75-103	Gowganda	Scott McLennan's collections. Huronian sequence	Mudstone	1.95-62.8	Gray clayey shale with silt laminae
SM-75-165	Gowganda	Scott McLennan's collections. Huronian sequence	Sandy mudstone	1.95-62.8	Dark gray clayey shale with silt-very fine sand laminae
SM-75-123	Pecors	Scott McLennan's collections. Huronian sequence	Mudstone	1.95-62.8	Dark gray clayey shale

Table 1. Rock samples used in this investigation.

- Formation listed unless collection source is unknown

The Huronian Supergroup sequence experienced deformation and low-grade metamorphism (sub-greenschist grade) during the Penokean Orogeny (1.85-1.80 Ga), resulting in meta-sedimentary rocks with recrystallization and albitization products. Mudstones from this sequence (**Table 1**) were initially geochemically and petrographically characterized by

McLennan et al., [1979], resulting in a petrographic perspective of mudstones with similar mineralogical content but obvious variations in matrix and framework mineral abundances. *McLennan et* al., [1979] categorized these mudstones into three broad groups based upon the content of their matrix and framework minerals: a sericite rich matrix group, a sericite rich matrix but framework mineral feldspar depleted group, and a chlorite rich matrix group. Also from this Huronian sequence sample set, a mixtite composed of poorly sorted, subrounded to angular quartz and feldspar very fine grains with a chlorite rich matrix (similar to the last group of mudstones) was analyzed.

Sample preparation is typically not required for thermal emission spectroscopy, but in order to cross analyze the same localities within each sample, freshly cut surfaces were prepared. I cut the samples to approximately 4.5 x 2.5 x 1.5 cm sizes to produce a thick section for TIR analysis. Thin sections from the same sample surface were analyzed by the other optical and microRaman point counting techniques. Thin sections were used for optical point counts and microRaman analysis in order to allow light to pass through the sample as well as mitigation of fluorescence caused by varying surface roughness.

3.2 Analytical Technique

3.2.1 Spectrometer Setup and Spectra Collection

Thermal emission spectra were collected at the Stony Brook University Vibrational Spectroscopy Laboratory using a Thermo Fisher Nicolet 6700 Fourier Transform Infrared (FTIR) Michelson interferometer that has been modified to directly measure emitted energy by removing the internal infrared (IR) source. The apparatus setup and the spectra collection technique follow closely to that of *Ruff et. al.,* [1997]. The sample's emitted radiation was acquired over a spectral range of 4000-200 cm^{-1} (2.5-50 μm) at a resolution of 4 cm^{-1}. During an

approximately eight minute acquisition period, 256 interferograms were collected at an optical velocity of 0.4747 cm^{-1}. Following an optical path directed by parabolic mirrors, emitted photons pass through a caesium iodide (CsI) beam splitter and are finally sensed by a deuterated triglycine sulfate (DTGS) detector. Rock samples were heated in an oven set at 80 °C for at least six hours. In order to increase the signal to noise ratio, samples were actively heated (80°C) throughout the acquisition period. The spectrometer and sample chamber (contained within a glovebox) are purged with air scrubbed of water vapor and CO_2, in an effort to mitigate the presence of water vapor and CO_2 absorptions in the measured spectra [*Ruff et al.*, 1997]. The sample chamber, constructed of copper and painted with high emissivity black paint in the interior, allows the environmental ("downwelling") radiance to be regulated by circulating water at a controlled temperature of 20 °C during the sample collection period [*Mathew et al.*, 2009]. Depending on sample size, the typical measurement spot diameter ranged from 1-1.5 cm, with coarser-grained samples requiring a larger spot size to accurately integrate compositional variability [*Michalski et al.*, 2004]. Before each session (four samples per session), the measurement of a warm and hot blackbody (70 °C and 100 °C, respectively) were obtained from a solid aluminum conical cavity (painted with high heat flat black paint) that was attached to the chamber apparatus [*Ruff et al.*, 1997]. The blackbody measurements are used to generate the instrument response function and calibrate the sample radiance measurement. This technique has been previously proven to have a reproducibility of better than 1% and an accuracy of better than 2%[*Ruff et al.*, 1997].

3.2.2 Spectral Modeling

The emissivity spectra of individual rock samples were modeled with mineral spectra using a nonnegative least squares method that was previously employed by *Rogers and*

Aharonson, [2008]. The nonnegative least squares method has been recognized to be a more reliable method than previous techniques because all library spectra remain in the matrix until a global minimum error is found resulting in a final nonnegative model fit [*Rogers and Aharonson*, 2008]. This method of linear least squares modeling requires a sample spectrum, a spectral library of potential end-members, and a wavelength range to operate on, and in turn, produces a best fit model of mixed library spectra, library spectra coefficients, end-members, and a root-mean-square (RMS) of the difference between the measured and modeled spectra. A spectral library from Arizona State University (ASU) developed by *Christensen et al.,* [2000] was modified to include all major phases that could potentially be present within a sedimentary rock. The library consisted of 129 mineral spectra collected from sand-sized or larger particles, or, for the case of clays, pressed pellets (**Table 2**). A black body end-member was also included to account for spectral contrast differences between rock and library spectra [*Hamilton et al*., 1997]. Mineral abundances were determined by subtracting the blackbody coefficient from the sum and re-normalizing the modeled library spectra coefficients to sum to 100% [*Feely and Christensen*, 1999; *Hamilton et al.*, 1997; *Wyatt et al.*, 2001]. In order to exclude the spectral signature of water vapor but include the major features characteristic of carbonates, the spectral modeling range for our samples was set from 1650-230 cm^{-1}, matching the wavelength range of our input library [*Hamilton and Christensen*, 2000]. Spectral plots in this work show the measured sample spectrum, the modeled spectrum, the individual end-member contributions to the model (scaled by modeled abundance) and the goodness of fit between the model and the measured in comparison to a zero reference point indicating perfect fit (**Fig 15. and 16**.).

Mineral Group	TIR Library ID *
Amphibole	Anthophyllite BUR-4760
	Glaucophane WAR-0219
	Hornblende BUR-2660
	Magnesiokatophorite ASU-03
	Pargasite HS-177.4B
	Tremolite var. jade (Nephrite) WAR-0979
Carbonate	Aragonite (long-axis oriented) C11
	Calcite (Iceland Spar) ML-C2
	Calcite C27
	Calcite C40
	Calcite ML-C10
	Cerussite C51
	Dolomite C17
	Dolomite C28
	Fe66Mg34CO3 C56
	Kutnahorite C43
	Magnesite C55
	Mg54Fe39CO3 C5
	Micrite, slope adjusted +
	Minrecordite C23
	Siderite C50
	Smithsonite C30
	Smithsonite ML-C1
	Witherite C52
Clinopyroxene	Augite BUR-620
	Augite HS-119.4B
	Augite NMHN-122302
	Augite NMNH-119197
	Augite NMNH-9780
	Diopside NMNH-107497
	Diopside WAR-6474
	Hedenbergite manganoan DSM-HED01
	Hedenbergite manganoan NMNH-R11524
	Hedenbergite WAR-HED01
Epidote	Epidote BUR-1940
Garnet	Almandine BUR-120A
Glass	Si-K_2O Glass + +
	Quenched Basalt + +
	Silica Glass + +
Halide	Flourite
	Flourite BUR-2080C
	Sylvite △
K-Feldspar	Anorthoclase WAR-0579
	Microcline BUR-3460
	Orthoclase WAR-RGSAN01
	Perthite WAR-5802
Mica	Biotite BUR-840
	Chlorite WAR-1924
	Clinochlore BUR-1340
	Muscovite WAR-5474
Olivine	Fayalite WAR-RGFAY01
	Forsterite AZ-01
	Forsterite BUR-3720A
	KI 3008 Fo10 ○
	KI 3115 Fo68 ○

	KI 3362 Fo60 ○
	KI 3373 Fo35 ○
	Bronzite BUR-1920
Orthopyroxene	Bronzite NMNH-119793
	Bronzite NMNH-93527
	Enstatite DSM-ENS01
	Enstatite NMNH-34669
	Enstatite NMNH-82436
	Enstatite NMNH-R14440
	Hypersthene DSM-FER01
Oxide	Magnetite WAR-0384
	Hematite BUR-2600
	Goethite-Derived Hematite GTSH2-300 □
	Specular Goethite WAR-G1, 710-1000 microns
	Syntheic Packed Goethite Powder GTS4 □
	Synthetic Packed Magnetite Powder MTS4 □
Phosphate	Apatite (perp. to c-axis) ML-P1
	Apatite ML-P1
	Apatite ML-P2
	Meta-variscite ML-P8
	Pyromorphite ML-P3
	Pyromorphite ML-P6
	Turquoise ML-P5
	Wavellite ML-P7
Plagioclase	Albite (Cleavelandite) WAR-0612
	Albite WAR-0235
	Andesine BUR-240
	Andesine WAR-0024
	Anorthite BUR-340
	Anorthite WAR-5759
	Bytownite WAR-1384
	Labradorite BUR-3080A
	Labradorite WAR-4524
	Labradorite WAR-RGAND01
	Oligoclase BUR-060
	Oligoclase WAR-0234
Quartz	Jasper
	Novaculite
	Quartz BUR-4120
	Qtz xtal a-axis (Herck-1)
	Qtz xtal c-axis (CT-1)
Serpentine	Serpentine HS-8.4B
Sheet-silicate	Ca-montmorillonite solid STx-1
	Fe-smectite solid SWa-1
	Kaolinite solid KGa-1b
	Illite granular IMt-2, scaled 130%
	Na-montmorillonite powder SWy-2
	Na-montmorillonite solid SWy-2
	Nau-1 < 0.2 mic ~ ~
	nau-2 < 0.2 mic ~ ~
	Nontronite solid WAR-5108
	Palygorskite solid PF1-1
	saponite <0.2 mic
	Sbdl < 0.2 mic
	SHca < 0.2 mic
	Swy-1 < 0.2 mic

Silica	02-011 Opal A ~
	02-015 Opal-CT/C ~
	Cristobalite ~
Sulfate	Anhydrite 755
	Antlerite ML-S10
	Barite ML-S2
	Bassanite 757
	Celestite ML-S3
	Gypsum 758
	Gypsum var. Alabaster ML-S11
	Anhydrous Magnesium Sulfate △
	Kieserite △
	Pentahydrite △
	Sanderite △
	Starkeyite △
Zeolite	Crystalline heulandite (zeo) x
	Crystalline stilbite (zeo) x

Table 2. Sedimentary mineral library composed of minerals spectra from the Arizona State University spectral library

* Except where indicated, all library spectra are from the ASU spectral library (tes.asu.edu) [Christensen et al., 200]

+ Hardgrove and Rogers, 2014

+ + Wyatt et al., 2001

△ Baldridge, 2006

□ Glotch et al., 2004

~ Michalski et al., 2003

~ ~ Michalski et al., 2006

x Ruff et al., 2006

○ Koeppen and Hamilton, 2008

3.2.3 Traditional Optical Point Counts

Modal composition from thin sections of samples with an average grain size of fine sand or larger (> 100 μm) was determined optically using a petrographic microscope. For any samples with a smaller average grain size, accurate identification of minerals by optical petrology becomes increasingly difficult [*Williams et al.*, 1954]. Sandstones were the main rock types meeting the criteria for a petrographic analysis; however, all samples were examined under a

petrologic microscope to qualitatively assess texture and grain size, as well as provide a rough independent check on abundances obtained through the other quantitative mineralogy techniques employed in this study. In total, 12 samples were examined by traditional point counting practices in order to establish their bulk mineralogy.

Sandstone petrographic methods have evolved over time with different techniques discussed in detail by [*Weltje and von Eynatten*, 2004]. For this study, the sample thin section was systematically scanned and approximately 250 grains were identified at an average step of 1.5 times the modal clasts grain size (unique to each sample), covering the entire 4.0 x 2.5 cm slide. Modal grain size was determined by averaging the diameter of clasts within each sample. Total rock composition was determined from the proportion that each mineral phase was identified within the ~250 points resulting in less than 6% absolute error, as determined from the chart for judging the reliability of point counting developed by *Van Der Plas and Tobi,* [1965]. This uncertainty is also comparable to the other quantitative techniques employed for bulk mineralogy within this study. Introducing a second point-counter to perform the analysis on two samples, as well as conducting multiple point counts on the same thin section for two samples, provided an estimate of operator error. These results yielded an error that was negligible to the final abundance results (< 5% absolute error).

Individual grains were optically identified beneath the cross hairs of the microscope and then classified into their respective sedimentary rock mineral phase. These mineral phases replicate the selection of library mineral spectra used as inputs to spectral models. Cement and matrix phases were generalized into a single "matrix" group based upon common optical features (i.e. texture, color, and grain boundary behavior) and are described in **Table 5**.

3.2.4 MicroRaman Point Counts

The method used for this procedure is a modified Raman point counting technique [*Haskin et al.*, 1997] that is specialized for mudstone classification. Individual mudstone samples have a relatively homogenous composition with a clay and silt fraction (1.95-62.6 μm) that require increased spatial resolution. In order to account for this texture in mudstones, smaller grids with an increased number of lines and points were used for this analysis. Raman micro-imaging spectroscopy was completed using a WITec alpha300R Micro-Imagining Raman spectrometer located at the Stony Brook University Vibrational Spectroscopy Laboratory. This system configuration combines a confocal microscope with a highly sensitive thermoelectrically cooled, back-illuminated CCD detector allowing for the detection of low intensity Raman shifts. In order to minimize scattering from an uneven surface, a double polished thin section was analyzed under a 50 X optical magnification. A 600 line/mm holographic grating spectrometer provides a 3 cm^{-1} spectral resolution between the region of 100-1650 cm^{-1}. Equipped with a piezoelectric stage, individual Raman spectra were collected at each pixel within a 175 x 175 μm grid resulting in 30,625 single point spectra. The spectrum at each spot (spot based upon magnification and for 50 X, spot size is sub-micron) was acquired using a 785 nm laser for 0.3 seconds. For each sample, grids were acquired at two random locations to increase sample representativeness, which resulted in an average difference of 12.5 vol %.

MicroRaman grids were corrected for cosmic ray interference and then the data were reduced to subtract the incident laser line. The resultant data cube was then processed in the Environment for Visualizing Images (ENVI) remote sensing software. To emphasize differences in spectral shape rather than overall magnitude, I normalized the spectra to the same maximum intensity value. I then performed a principal components analysis (PCA) on the normalized

spectra to better identify the major components in each sample and define regions of interest for pixel-based spectral classification. Through trial and error, I determined that 7-10 regions of interest adequately captured the spectral variability found in our samples. Given that a typical mudrock is usually composed of 5-6 components (clay, micas, quartz, feldspar, carbonates, and organic matter [*Blatt et al*., 2006]) use of 7-10 regions of interest is a conservative number that ensures no components are missed. The regions of interest were used as an input into a maximum likelihood supervised classification [*Richards and Jia*, 2006], which uses the region of interest statistics to determine the probability that any given pixel within the data cube falls into the same data distribution as the region of interest. In this work, I used a probability threshold of 95%; pixels with values below this probability threshold were not classified. Typically, 3% of pixels in each data cube were not classified. To reduce data redundancy and work only with components with real signal (as opposed to noise), I performed the classification using only the top 15 PC bands. After the initial classification step, I analyzed the class mean spectra and merged classes with similar class mean spectra, including the unclassified mean spectra. The symmetrical center peak positions of the final class means were visually located. Peak shift positions were then used to determine the dominant phase (s) in each class by referencing the well-characterized library standards available from the RRUFF database at the University of Arizona. Multiple mean class spectra displayed features consistent with a combination of minerals. Previous studies have divided abundances within these multi-phase spectra equally [*Ling et al.*, 2011], but this may result in incorrect abundance estimates that do not justify this extra step. For this work, I identified each potential phase present in the mixed spectra and then quantified the abundance of the phase assemblage as a whole. Finally, abundances of each phase were determined by summing the number of pixels in each class and dividing by the total

number of pixels in each data cube. Like the thermal emission spectral models and the optical point count methods, this technique produces a volume abundance, rather than a weight percent abundance.

3.2.5 Quantitative X-ray Diffraction

Powdered X-ray diffraction was completed using a Rigaku SmartLab Automatic X-ray Diffractometer system located at NASA's Ames Research Center in Moffett Field, California. The sample was homogenized into a fine powder (<20 μm) and an XRD pattern was acquired using a side-loaded orientation, which has been proven in previous work to lead to more reproducible results (particularly when a clay fraction is present) [*Srodon et al*., 2001]. After phase identification from XRD profiles, mineral abundances were determined by using the Rietveld refinement technique [*Rietveld,* 1969] as implemented using the BGMN program [*Bergman et* al., 1998]. BGMN allows modeling of partially disordered clay minerals [*Ufer et al*., 2004] in addition to crystalline phases. XRD weight abundances were then converted to volume abundances in order to allow for a direct comparison to the other techniques used in this study.

4. Results

4.1. TIR Modal Mineralogy

Figure 1 shows the TIR spectra of 12 sandstones and 15 mudstones that were analyzed in this work. **Tables 3** and **4** list the modeled results for bulk mineralogy and **Figures 4** and **5** display the modeled and measured spectra, mineral phases contributing to the model (in proportion to their volume abundance). Mineral abundances are normalized to 100% after subtracting modeled blackbody abundances (mudstones ranging from -66.92 to 12.06% and

sandstones -21.33 to 34.80%). **Figure 2** displays the frequency of all library endmembers with a derived abundance greater than 3% that were used in the linear models. Mineral abundances below this value are near the detection limit for the most strongly absorbing minerals and are therefore excluded from the results [*Ramsey and Christensen*, 1998; *Rogers and Aharonson*, 2008]. A comparison between all sandstone and mudstone spectra (**Figure 1**) highlights the bulk mineralogical changes that are observable in the TIR.

On average, sandstone models identified between 8-9 mineral phases per sample and mudstone models recognized between 11-12 mineral phases. Examples of the most common library spectra used in the unmixing algorithm are displayed in **Figure 3**. The vibrational motion that occurs is significantly different for each group and thus allows for easy identification within measured spectra [*Christensen et al.*, 2001]. This figure does not encompass the variability within each group but instead provides a framework to discuss the goodness of fit (or lack there of) between the bulk rock and modeled spectra.

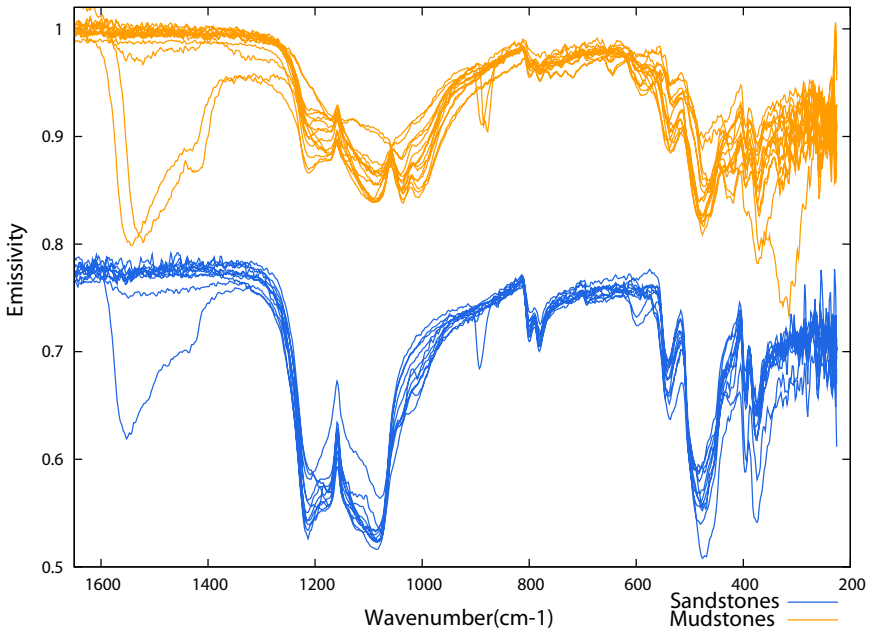

Figure 1. The measured emissivity spectra for all sandstone and mudstone samples. Major differences between sandstone and mudstone TIR spectra are mainly observed from ~1250-1000 cm^{-1}, primarily due to differences in clay abundance. Carbonate features are present in some samples between ~1550-1450 cm^{-1}. The prominent absorptions between ~1300-1050 cm^{-1} are due to quartz.

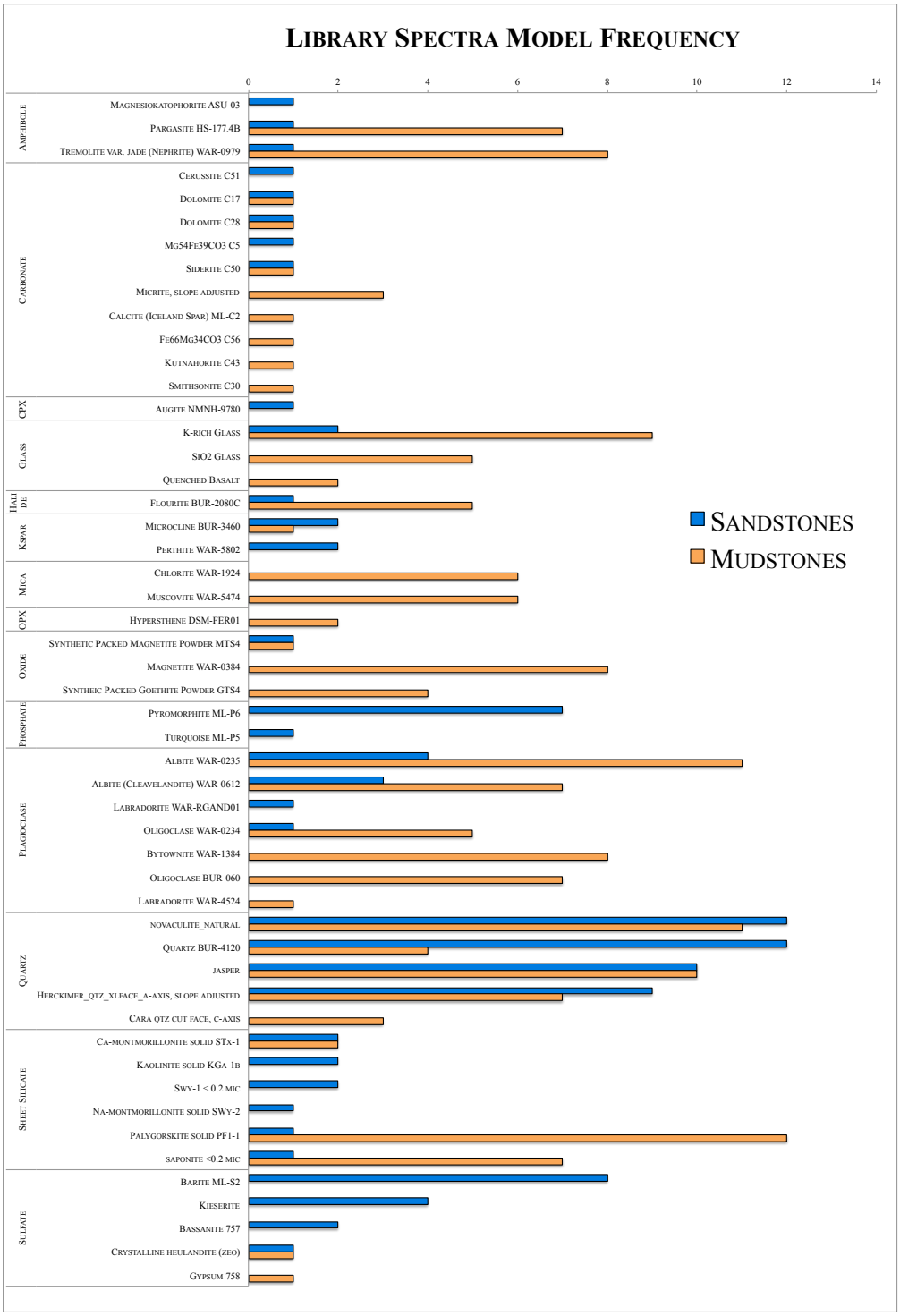

Figure 2. Frequency of use in the unmixing models (at an abundance of ≥ 3 vol %), for each TIR library spectrum. Library spectra are identified by their ID name and divided into their respective groups. The most frequently identified mineral phase for mudstones was palygorskite and for sandstones was novaculite and quartz. The most frequently modeled mineral group for mudstones was plagioclase and for sandstones it was quartz.

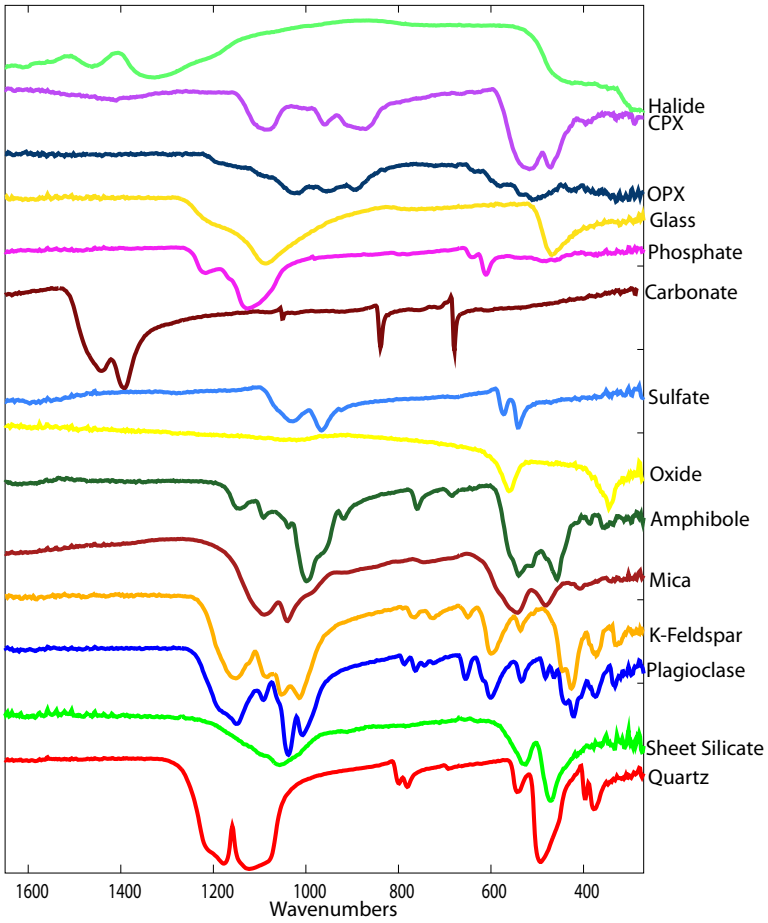

Figure 3. Emissivity spectra from specific library mineral phases that were commonly identified using the nonnegative least square method.

4.1.1 Sandstone TIR

Thermal infrared emission spectra of sandstones display absorptions that are characteristic of the component crystal structures and can be generalized based on wavelength position and shape (**Figure 4**). All sandstones have very similar spectral shapes as a result of the fundamental vibration of anion groups. The prominent absorption doublet that occurs between ~1300-1050 cm^{-1} in all of the measured sandstone spectra is due to quartz. However, there is a variation between the U versus V shape of these absorptions, which can be attributed to the

characteristic difference between macro- and microcrystalline quartz [*Hardgrove and Rogers*, 2014]. Also observed in the same spectral region (sample dependent) are notable deviations from the typical quartz doublet, which can be influenced by contributions from sheet silicate, sulfate, or plagioclase phases.

	16.606	La Boca	Mis-Te-2	Tx-Te-1	Devil K	D1-72-91	Catskil Sk-1	Smithwick	Flat Irons	Bera	Gratton	Mt. Tom
Amphibole	6.7 ±0.8	12.3 ±1.4	2.6 ±0.5	1.6 ±0.5	0.0	2.0 ±0.9	1.8 ±0.9	1.7 ±0.9	0.0	0.0	0.0	1.5 ±0.7
Carbonate	4.3 ±0.5	1.5 ±0.4	1.8 ±0.2	1.3 ±0.3	0.4 ±	1.4 ±0.4	1.9 ±0.6	1.8 ±0.3	1.6 ±0.2	7.6 ±0.6	41.5 ±0.7	1.4 ±0.4
CPX	0.0	5.8 ±1.9	2.6 ±0.4	0.0	2.0 ±	0.0	0.0	0.0	0.0	0.0	0.0	0.0
Garnet	0.0	0.2 ±0.4	0.0	0.0	0.0	0.0	0.0	0.0	0.0	0.0	0.0	0.0
Glass	0.0	0.0	0.0	15.6 ±1.5	0.0	0.1 ±2.2	10.2 ±1.7	1.3 ±1.3	0.0	0.0	0.0	0.0
Halide	1.8 ±0.3	5.2 ±0.3	0.0	0.2 ±0.2	0.0	0.0	0.2 ±0.3	0.0	0.0	0.2 ±0.3	0.0	0.0
K-Feldspar	0.0	0.0	0.0	1.3 ±0.9	0.0	6.8 ±1.6	0.0	0.0	27.8 ±0	0.0	0.0	7.7 ±2.4
Mica	1.1 ±0.6	0.0	0.0	0.0	0.0	0.0	2.1 ±0.7	0.0	0.0	0.0	0.0	0.0
Olivine	0.0	0.0	0.0	0.7 ±0.3	0.0	0.0	0.0	0.0	0.0	0.0	0.0	0.0
Oxide	0.2 ±0.4	7.0 ±1.4	1.1 ±0.2	0.3 ±0.2	1.0 ±	0.1 ±0.3	2.0 ±0.6	1.2 ±0.3	0.1 ±0.3	0.0	0.7 ±0.3	0.1 ±0.3
Phosphate	5.3 ±1.3	0.0	10.0 ±0.9	0.5 ±0.9	4.1 ±	0.0	8.0 ±1.2	5.1 ±0.9	4.0 ±0	0.0	0.0	4.0 ±1.4
Plagioclase	5.0 ±1.0	7.8 ±1.1	0.8 ±0.4	9.2 ±1.4	0.2 ±	29.6 ±2.6	0.9 ±0.6	1.8 ±0.9	7.6 ±1.9	0.0	0.0	23.1 ±2.0
Quartz	56.5 ±0.5	41.7 ±0.5	59.5 ±0.3	39.8 ±0.5	74.9 ±	54.0 ±1.0	61.3 ±0.6	77.3 ±0.5	44.8 ±0.5	69.3 ±0.5	51.6 ±0.4	44.0 ±0.4
Clay	9.0 ±1.1	18.5 ±1.8	12.9 ±0.5	16.7 ±1.5	4.0 ±	0.0	9.6 ±3.3	4.5 ±3.3	10.4 ±1.4	0.0	0.0	0.0
Silica	0.0	0.0	0.0	1.7 ±0.9	0.0	0.0	0.0	0.0	0.0	0.0	0.0	0.0
Sulfate	10.2 ±1.0	0.0	8.8 ±0.7	7.7 ±0.9	13.4 ±	5.8 ±1.5	1.9 ±1.1	5.3 ±0.8	3.5 ±0.8	22.9 ±0.9	6.2 ±0.8	18.1 ±1.2
Zeolite	0.0	0.0	0.0	3.3 ±1.9	0.0	0.2 ±3.6	0.0	0.0	0.0	0.0	0.0	0.0

Table 3. Mineral abundances and the statistical errors for sandstone samples, derived from the nonnegative unmixing algorithm

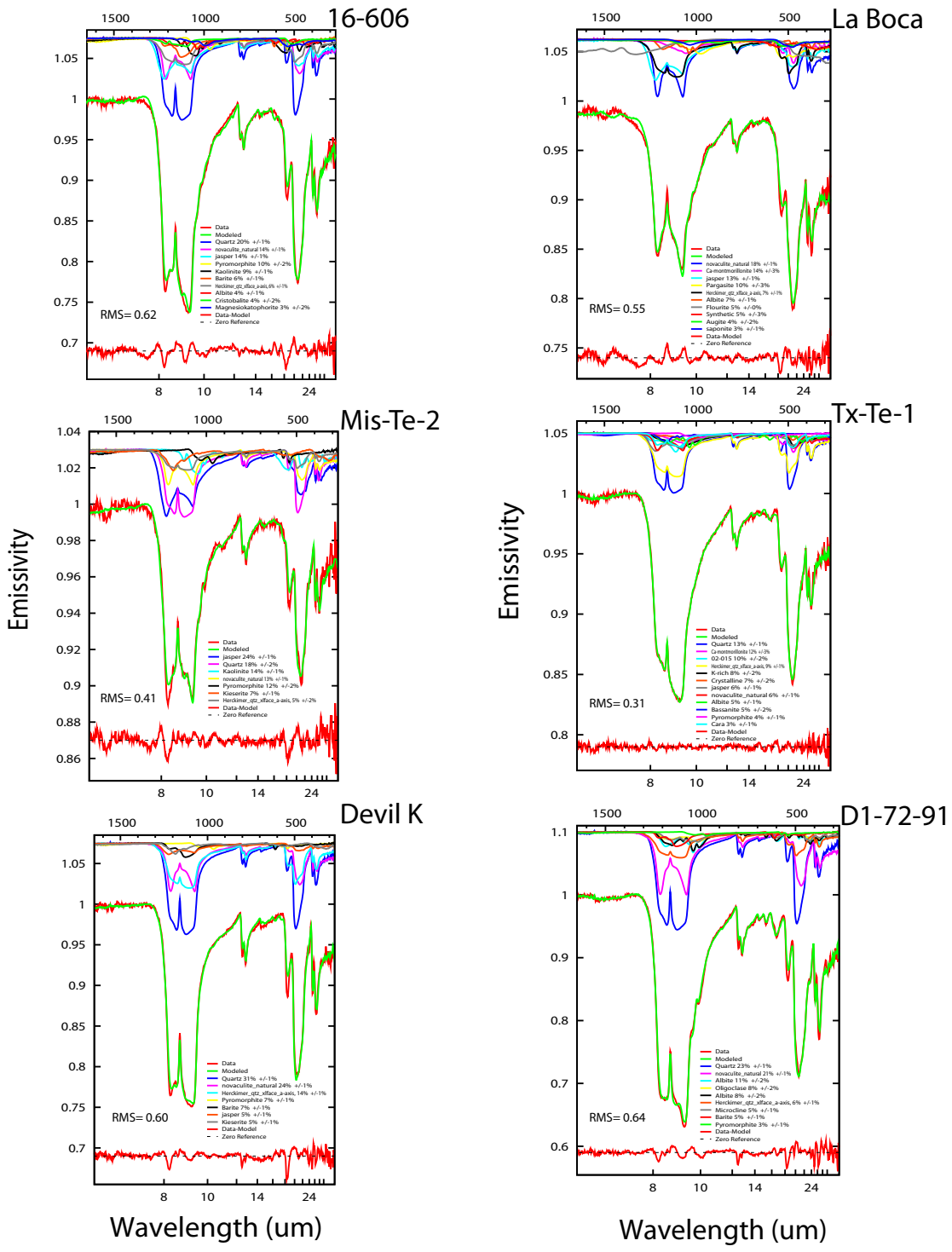

Figure 4. Measured vs. modeled TIR emission spectra of 12 sandstones. Only individual mineral phases with abundances ≥ 3 vol % are displayed. In general, RMS values indicate a good fit between the measured and modeled spectra. Any deviation from a one-to-one relationship is highlighted using a zero reference line.

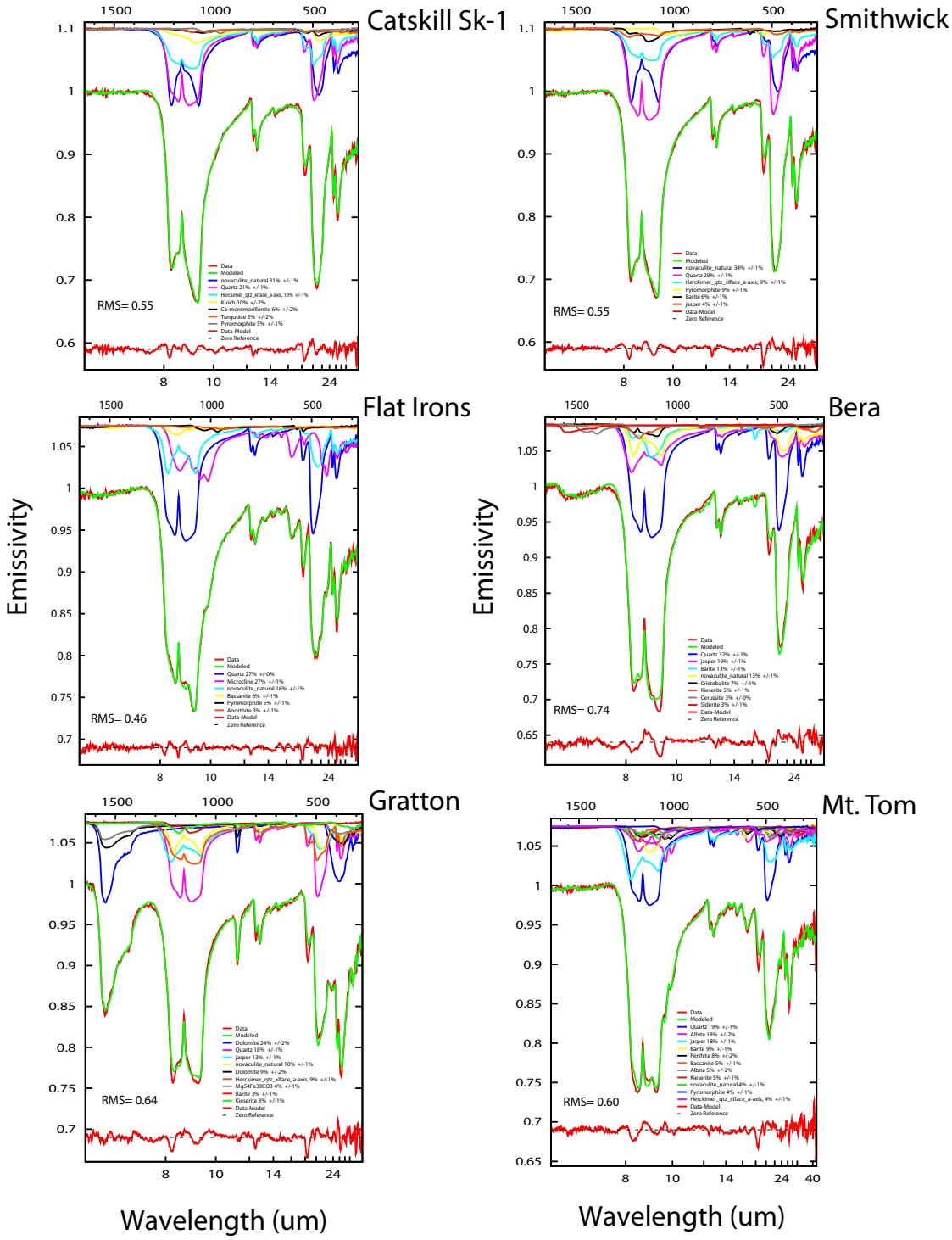

Figure 4. Continued

The most frequently modeled mineral group (greater than 3% abundance) derived from the sandstone unmixing algorithm was quartz. On average, quartz abundances (including macro- and microcrystalline phases) were modeled at 56 vol % with a range from 40 to 77 vol %. Both macrocrystalline (Quartz BUR-4120) and microcrystalline (Novaculite-Natural and Jasper) were modeled in each sandstone spectrum. After quartz, the most abundant mineral groups used in the models were sheet silicates, plagioclase and alkali feldspars, carbonates, phosphates and sulfates. Mineral abundances and individual phases were sample dependent, but in general two albite library members (Albite WAR-0235 and Albite Cleavelandite WAR-0612) were commonly identified from the plagioclase series and microcline (Microcline BUR-3460) was most frequently used alkali feldspar phase. Kaolinite (Kaolinite solid KGA-1B) and montmorillonite (both Ca- and Na-montmorillonite solid) were the most readily used sheet silicate members, whereas Barite (Barite ML-S2) was repeatedly modeled from the sulfate group. Mica and hematite abundances were low (< 2%) in most models.

Though spectral differences between the bulk rock and the model fits are generally low, there are noticeable areas of misfit that can be generalized into two wavenumber groups between ~1150-1250 cm^{-1} and ~500-600 cm^{-1} (**Figure 4**). Root mean square (RMS) values are a function of the goodness of fit between the measured and modeled and therefore unique to physical characteristics and complexity of each sample. The average RMS value for sandstones was 0.56%.

4.1.2 Mudstone TIR

Plagioclase was modeled with the highest average abundance of 23 vol % and was used in every mudstone spectral model. Albite was the most frequently identified plagioclase phase,

but also identified in the solid solution series were bytownite, oligoclase, and labradorite. Micas, in particular muscovite and chlorite, were used in almost every model and had an average derived abundance of ~ 6 vol%. Clays and quartz were the next most frequently used mineral groups and displayed abundances between 14-18 vol %. Microcrystalline quartz was the more commonly identified quartz phase, whereas palygorskite was the most commonly modeled clay. Glass phases, mainly a SiO-K glass similar to obsidian (listed as "K-rich glass" in Figures 2, 4, and 5), was used in 80% of the unmixing models and accounted for an average abundance of ~ 12 vol%. Oxide, amphibole, and carbonate phases were often used in the model fits and collectively accounted for an average abundance of ~20 vol%.

	SM-75-117	**SM-75-134**	**SM-75-158**	**SM-75-107**	**SM-75-152**	**SM-75-161**	**SM-75-167**	**SM-75-104**	**SM-75-120**	**SM-75-142**	**SM-75-105**	**SM-75-113**	**SM-75-165**	**SM-75-103**	**SM-75-123**
Amphibole	12.2 ± 1.1	9.6 ±1.4	0.0	0.0	8.9 ±1.0	0.0	0.0	9.3 ±1.6	15.5 ±1.5	8.8 ±1.3	5.1 ±1.1	11.4 ±2.1	2.1 ±0.8	5.4 ±1.4	8.1 ±1.3
Carbonate	2.4 ±0.5	2.6 ±0.5	46.4 ±0.7	3.8 ±0.7	6.1 ±0.7	26.4 ±0.8	3.0 ±0.5	4.5 ±0.8	3.4 ±0.4	3.3 ±0.6	5.4 ±0.7	1.7 ±0.6	2.8 ±0.8	2.5 ±0.6	2.2 ±0.5
CPX	0.0	0.0	0.0	0.0	0.0	0.0	0.0	0.0	0.0	0.0	0.0	0.4 ±0	0.0	0.0	0.0
Garnet	0.0	0.0	0.0	0.4 ±0.4	0.3 ±0.3	1.1 ±0.4	0.6 ±0.5	0.2 ±0	0.0	0.0	1.3 ±0.4	0.0	1.3 ±0	0.0	0.0
Glass	0.0	0.0	0.0	36.4 ±5.3	12.8 ±2.2	11.5 ±1.7	34.8 ±3.8	13.4 ±2.9	4.8 ±1.2	6.2 ±2.9	12.2 ±1.5	11.6 ±2.1	23.4 ±2.9	10.6 ±1.9	5.3 ±1.6
Halide	1.3 ±0.2	2.1 ±0.3	3.0 ±0.2	4.2 ±1.0	6.4 ±0.3	4.3 ±0.2	3.9 ±0.8	2.2 ±0.9	2.1 ±0.2	2.5 ±0.3	2.0 ±0.9	0.0	2.4 ±0.8	2.0 ±0.3	2.7 ±0.3
K-spar	0.0	0.0	0.0	1.6 ±1.2	0.0	3.4 ±0	2.1 ±0	0.0	0.0	0.0	0.0	0.0	0.8 ±0	0.0	0.0
Mica	6.4 ±0.6	7.6 ±0.7	0.0	5.4 ±1.3	3.9 ±1.3	1.3 ±0.7	3.9 ±1.0	3.1 ±2.5	12.5 ±0.5	12.4 ±0.8	5.2 ±0.8	5.0 ±0.7	4.7 ±0.6	5.7 ±2.1	8.2 ±0.9
OPX	0.0	0.0	0.0	0.0	0.0	0.0	0.0	0.0	0.0	0.0	0.0	0.0	0.0	8.9 ±0	11.6 ±0
Oxide	1.4 ±0.6	2.8 ±1.0	0.0	4.9 ±1.7	5.5 ±1.0	0.0	9.2 ±1.3	8.9 ±1.8	6.6 ±1.1	5.3 ±1.6	5.3 ±1.2	8.2 ±0.6	6.7 ±1.3	9.9 ±1.3	6.0 ±1.2
Phosphate	1.2 ±0	0.0	3.2 ±0	0.0	0.4 ±0	0.0	0.0	0.0	0.5 ±2.3	0.7 ±0	0.0	0.0	0.0	0.0	0.0
Plagioclase	8.8 ±1.5	26.0 ±0.7	11.5 ±3.7	36.4 ±1.6	19.7 ±1.8	25.6 ± 2.8	34.1 ±2.2	20.1 ±1.7	7.4 ±0.8	8.9 ±2.0	51.1 ±1.9	14.7 ±1.9	43.6 ±2.9	18.3 ±2.3	18.7 ±0
Quartz	51.7 ±0.5	32.3 ±0.5	17.1 ±0.5	2.2 ±0.7	14.0 ±0.6	7.0 ±0.6	2.8 ±0.6	9.0 ±0.8	30.3 ±0.6	18.8 ±1.0	12.4 ±0.7	29.0 ±0.7	12.2 ±0.6	11.7 ±0.9	15.2 ±0.7
Clay	12.6 ±3.1	16.5 ±3.7	3.6 ±2.0	4.3 ±3.9	20.3 ±2.9	19.1 ±2.5	5.7 ±3.0	27.9 ±4.8	16.9 ±3.3	29.2 ±4.0	0.0	18.0 ±0	0.0	24.9 ±3.8	21.8 ±0
Silica	0.4 ±0.2	0.1 ±0.2	0.5 ±0.3	0.4 ±1.6	1.8 ±0.2	0.4 ±0	0.0	1.2 ±0.2	0.1 ±1.9	0.8 ±0	0.0	0.0	0.0	0.0	0.0
Sulfate	1.7 ±0.8	0.4 ±1.2	5.6 ±0.7	0.0	0.0	0.0	0.0	0.0	0.0	3.2 ±0	0.0	0.0	0.0	0.0	0.0
Zeolite	0.0	0.0	9.0 ±0	0.0	0.0	0.0	0.0	0.0	0.0	0.0	0.0	0.0	0.0	0.0	0.0

Table 4. Mineral abundances and statistical errors for mudstone samples, derived from the nonnegative unmixing algorithm

Spectral comparison between the measured and model results display a particularly good fit (**Figure 5**). There are subtle misfits between the bulk rock spectra and the modeled spectra, but overall the result is an average RMS value (0.56%) that is identical the sandstone models average RMS value (0.56%). Spectral shapes can be generalized based on mineral group contributions. Feldspar features are displayed in the ~ 1300-950 cm^{-1} region. The common quartz doublet in the same region is less prominent in the mudstones compared to sandstones, except for sample SM-75-117. Carbonate emission features are detected in the ~ 1550-1450 cm^{-1} region for some samples and are most consistent with the dolomite phase. Magnetite was the most common iron oxide modeled, and displays its contribution to the modeled spectra between ~500-300 cm^{-1}.

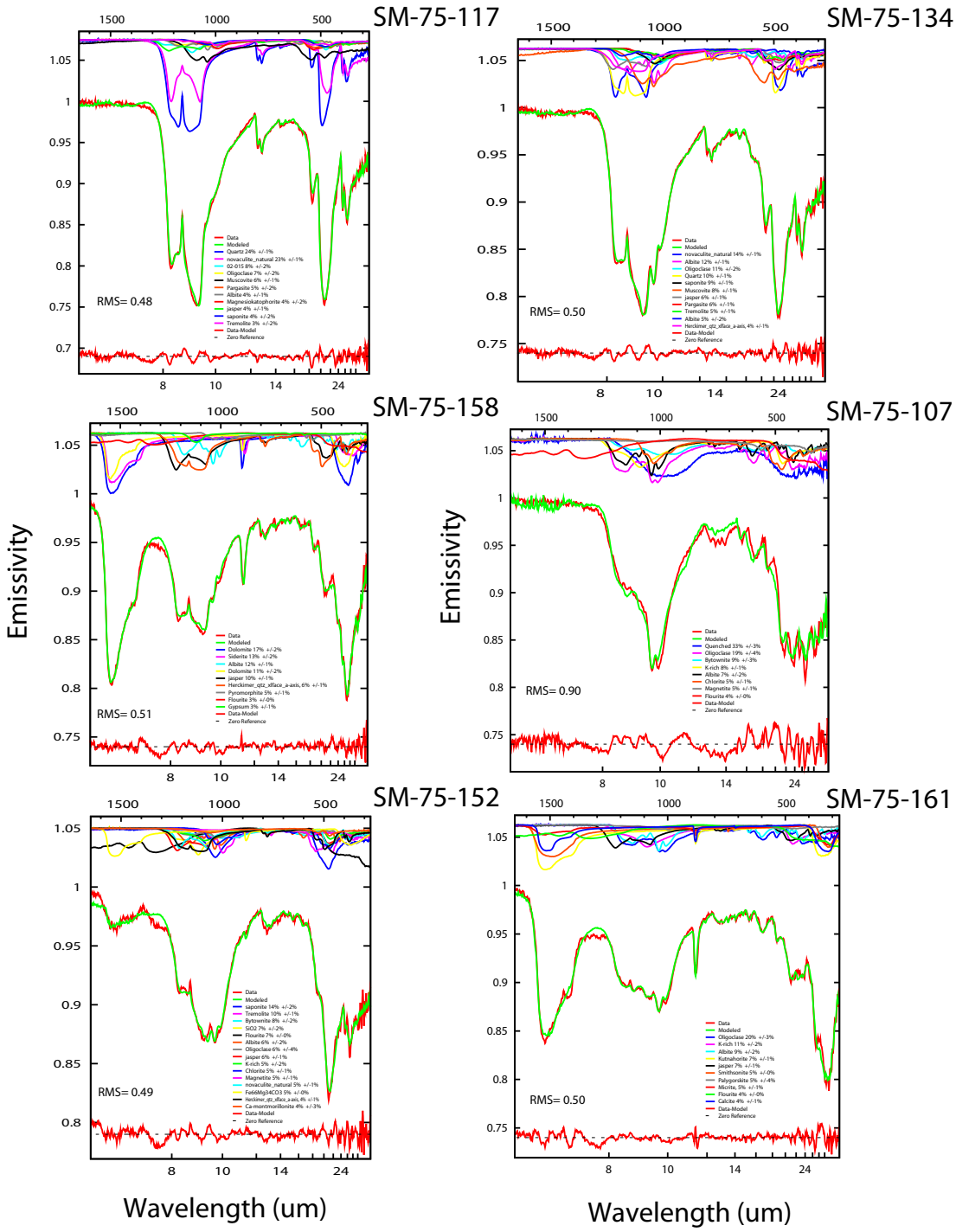

Figure 5. Measured vs. modeled TIR emission spectra of 15 mudstones. Only individual mineral phases with abundances ≥ 3 vol % are displayed. In general, RMS values indicate a good fit between the measured and modeled spectra. Any deviation from a one-to-one relationship is highlighted using a zero reference line

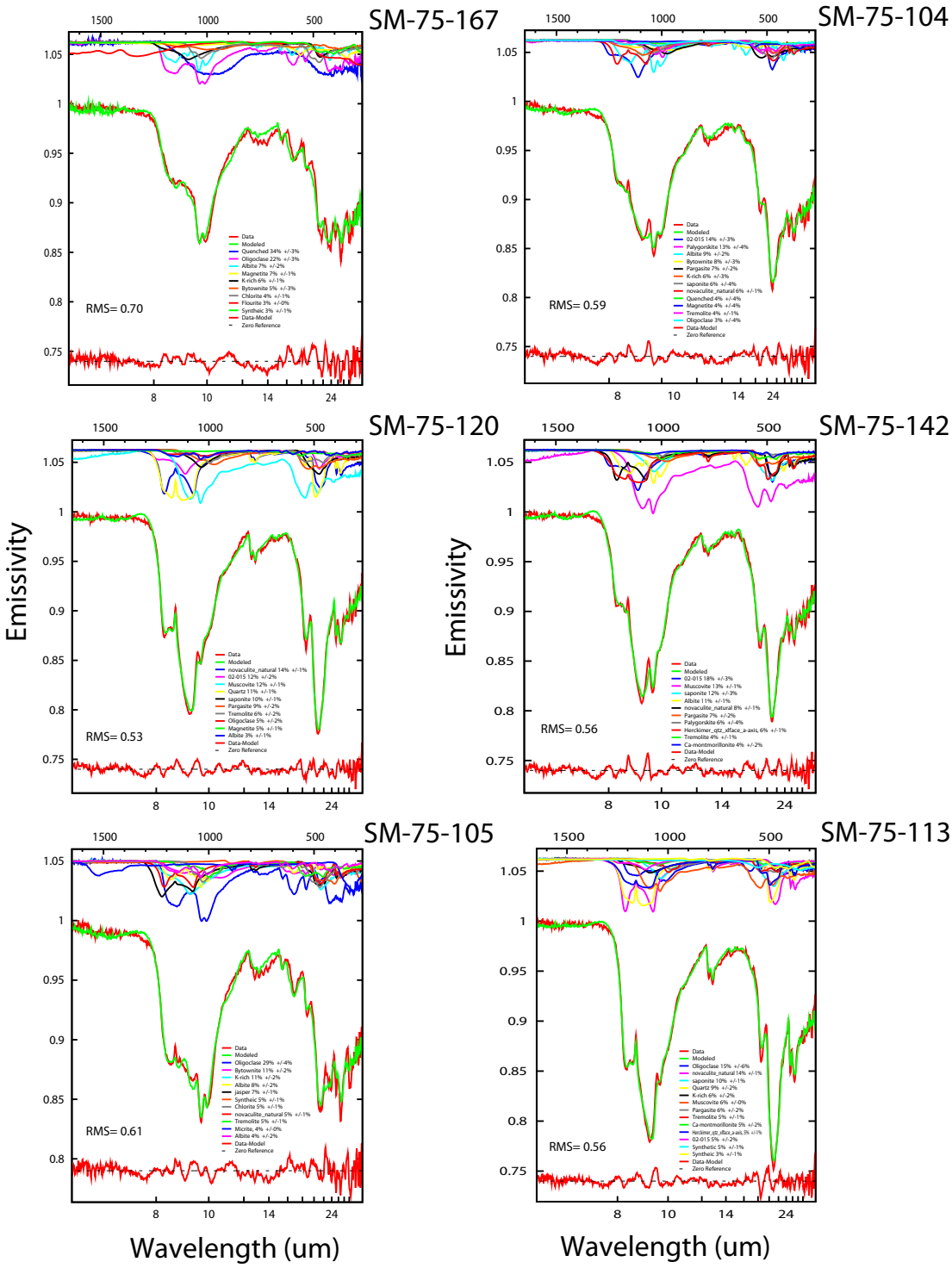

Figure 5. Continued

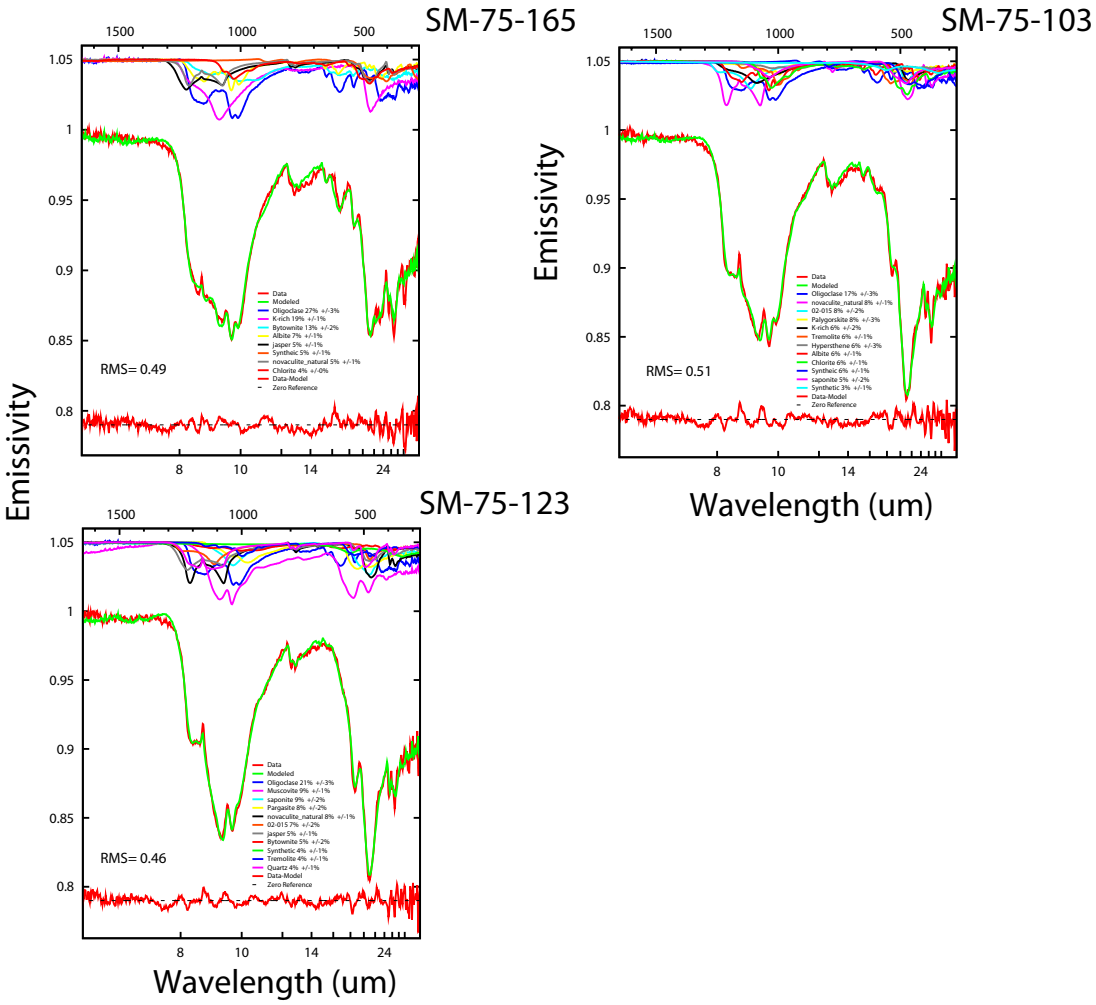

Figure 5. Continued

4.2. Sandstone Point Counts

Mineral abundances derived from thermal emission models for sandstones were compared to the traditional optical petrologic technique of thin section analysis using a point counting procedure. Modal mineralogy determined from point counts (**Table 5**) was conducted prior to acquisition of TIR spectra to avoid bias. We broke mineral identification down into six classes: quartz, plagioclase feldspar, potassium feldspar (Kspar), micas, "lithics plus", and matrix minerals. The first four mineral classes are considered the framework minerals, and the optical

identification of these minerals is straightforward with the use of a petrologic microscope. Traditionally, grains counted as lithic fragments consist of any polymineralic pieces of a preexisting rock that has weathered down to a sand-sized grain and incorporated into the sandstone rock. In these cases, the lithic fragment compositions are qualitatively assessed because the origin of preexisting rock can give substantial insight to provenance. However, in this work, a "lithic plus" group was created to include lithic fragments, oxides, and accessory minerals, due to the minor volume percentage each group member accounted for. Though this presents some ambiguity for direct comparison to TIR spectral models, this group accounts for < 5% of counted grains, and this should not have a significant impact on the comparisons. Lastly, our matrix class consisted of any mineral grains that were smaller than 30 μm and filled the interstitial spaces between the framework minerals of the first four classes, including matrix grains and cement. The common definition for matrix is the groundmass of detrital grains that are smaller than 30 μm, whereas cement typically refers to the mineral precipitated from diagenetic fluids that replace the void space between grains [*Blatt et al*., 2006]. The identification of matrix components can be extremely difficult with the standard petrologic approach. Also, the differentiation of matrix versus cement in sandstones can be highly ambiguous. For this reason, the matrix group was created to incorporate all fine-grained material below the detection capability of a petrologic microscope. The matrix group was also qualitatively assessed based upon distinguishing optical features and generalized components, which are listed in **Table 5**. Common matrix material consisted of clay, finely grained micas, chlorite, quartz, hematite, and calcite.

	D1-72-92	Tx-Te-1	Mis-Te-2	Catskill Sk-1	La Boca	16-606	Devil K	Smithwick	Bera	Flat Irons	Mt. Tom	Gratton
Quartz	55	52	58	64	45	56	73	71	66	51	47	48
Plagioclase	9	3	0	6	12	2	0	1	0	3	29	16
Kspar	17	8	2	6	1	0	0	1	0	27	7	0
Micas	0	3	3	1	7	4	0	1	2	2	2	3
Lithics Plus	0	5	2	0	4	1	1	0	0	0	2	3
Matrix	18	29	35	23	31	35	25	26	31	17	13	29
Matrix Components	Calcite Cement	Clay Matrix	Hematite Cement	Calcite Cement	Clay Matrix	Clay Matrix	Chlorite, Carbonate, and Quartz	Clay Matrix	Micaeous Clay	Micaceous Clay	Iron Rich Clay	Chlorite, rock flour matrix

Table 5. Sandstone mineral abundances determined from traditional point counts

For consistency, we performed the thin section analysis at the same area that the spectral measurements were taken. Photomicrographs of samples in plane- and cross-polarized light are displayed in **Figure 6**.

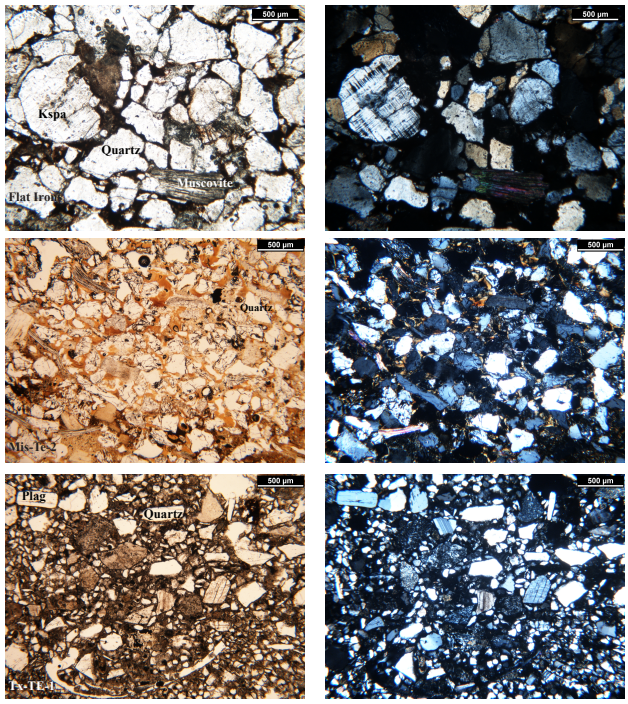

Figure 6. Three photomicrographs of selected sandstone samples, displayed in both plane- and cross-polarized light (left and right photos, respectively). Point counts were conducted on the sandstone samples and served as the "known" comparison to TIR modeled abundances. Framework clasts, i.e., quartz, feldspar, and muscovite are easily identified. Matrix material (< 30μm) and cements are distinguished

qualitatively by texture and color. Flat Irons has a micaceous clay rich matrix. Mis-Te-2 has a hematite rich cement, and Tx-Te-1 has a clay rich matrix.

4.3 Sandstone Classification

The mineral composition of the sandstones examined is simplified in the ternary plot displayed in **Figure 7**. The triangular plot creates a classification scheme relating the total quartz, feldspar, and the other mineral/lithic abundances to serve as a comparison between the petrographically determined abundances (circles) and the TIR derived abundances (same color triangles). The "other" class in the bottom right pole includes all other mineral phases besides quartz and feldspar. This generalization for TIR mineral abundances may inherently result in incorrect estimation of mineral phases, because the matrix may also include quartz and feldspar. However, for the sake of comparison, it serves as a valuable assumption to assess bulk mineralogy results.

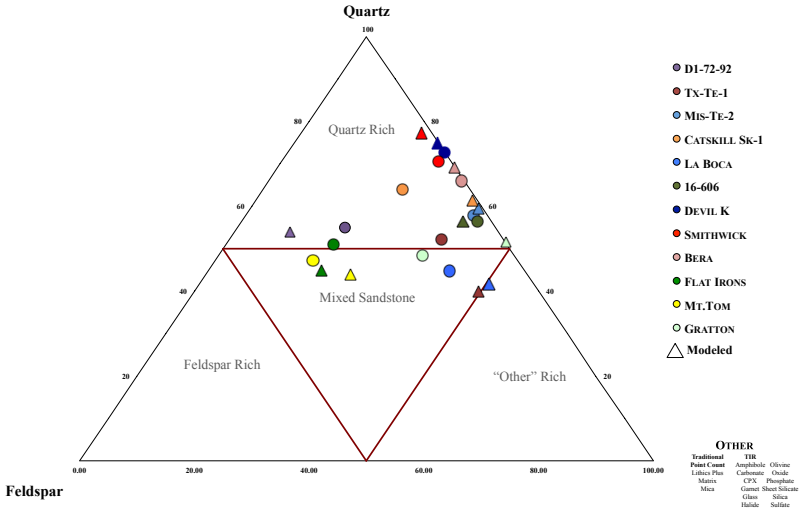

Figure 7. A ternary plot of sandstone classification comparing the measured abundances obtained from traditional point counts (circles) with the modeled abundances derived from TIR spectral models (triangles). With the exception of four samples, both traditional point counts and TIR spectral models result in the same rock classification.

4.4 MicroRaman Derived Abundances

Raman spectroscopy results for mudstone samples are displayed in **Table 6**. Photomicrographs of characteristic samples are displayed in plane-and cross-polarized light (**Figure 8**), in order to highlight textural differences between mudstone samples. Six mineral classes were defined based on spectral detection in the Raman data: quartz, plagioclase, micas, "highly fluorescent", "oxides plus", and "undifferentiated". **Figure 9** displays the steps leading to the selection of regions of interest and **Figure 10** displays a classification map along with the spectra of each six mineral classes used for identification. The most common library mineral phases that were used to identify components of the measured mudstone spectra are displayed in **Figure 11**, along with a simplified representation of key Raman shift locations.

	SM-75-103	**SM-75-104**	**SM-75-105**	**SM-75-107**	**SM-75-113**	**SM-75-117**	**SM-75-120**	**SM-75-123**	**SM-75-134**	**SM-75-142**	**SM-75-152**	**SM-75-158**	**SM-75-161**	**SM-75-165**	**SM-75-167**
Quartz	23.35	10.8	26.29	2.49	34.15	36.05	46.35	35.7	56	11.55	17.45	31.7	0	4.9	4.75
Plagioclase	0	4.75	6.05	14.56	2.35	0.90	0	0	0	9.56	4.2	1.91	6.53	0.05	7.77
Micas	1.4	0	0	0	0	0	0	0	17.15	0	1.1	1.42	6.47	0	0
Oxides plus	0.95	11.75	0	1.4	14.15	2.28	2.2	5	2.05	2.43	4.88	8.79	4.85	3.5	3.13
Highly Fluorescent	10.95	11.55	45.65	12.19	2.95	0	0	0.65	1.2	0	1.45	0	6.55	8.5	0.5
Undifferentiated	63.5	60.95	22.05	69.3	46.45	60.79	51.45	58.3	23.45	76.48	70.1	56.13	75.74	83.05	83.83
Undifferentiated Components	Micas, Clays and Quartz	Micas, Clays and Quartz	Micas, Clays and Quartz	Micas, Clays and Quartz	Micas, Clays and Quartz	Micas, Clays and Quartz	Micas, Clays and Quartz	Micas, Clays and Quartz	Micas, Clays and Quartz	Micas, Clays and Quartz	Micas, Clays and Quartz	Micas, Clays and Quartz	Micas, Clays and Quartz	Micas, Clays and Quartz	Micas, Clays and Quartz

Table 6. Mudstone mineral abundances determined from microRaman point counts

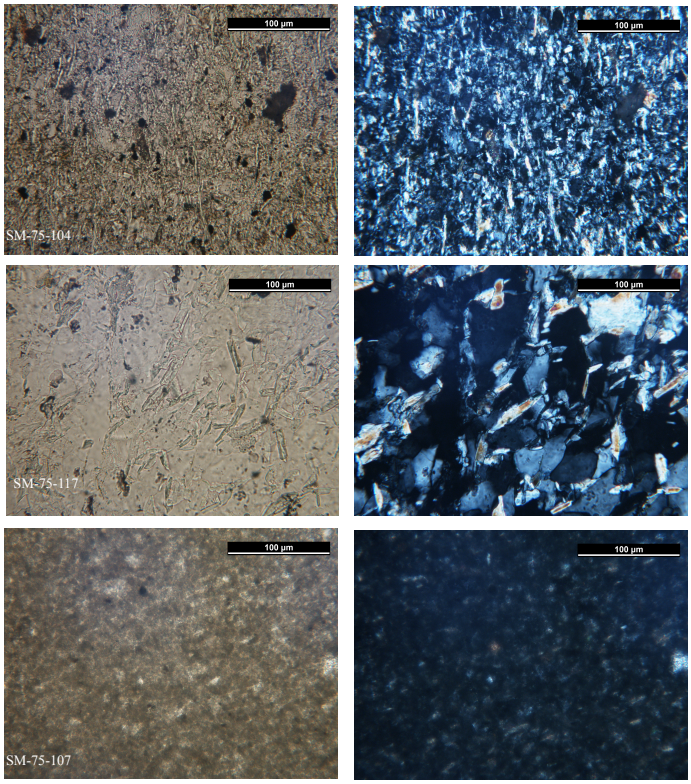

Figure 8. Mudstone photomicrographs of three selected samples are displayed in plane- and cross-polarized light (left and right photos, respectively). The small grain size (typically < 62.5µm, with the majority < 30µm) makes traditional point counting procedures inadequate. Therefore, mudstone samples were examined using microRaman spectroscopy.

The first three classes consist of the framework minerals in mudstones and display sharp and distinct Raman shifts consistent with well crystalline single grains. The fourth class, "oxides plus", includes low abundance detrital grains (oxides and clinopyroxenes). Oxides, and in particular, titanium oxides were present in most samples. Clinopyroxene was observed in only two samples.

"Highly fluorescent" is a broad category that encompasses any material that exhibits high fluorescence and results in Raman intensities near the incident laser light intensity. This in turn mask phase identification across large portions of the spectrum and thus makes mineral

classification extremely difficult (**Figure 10**). In natural samples, common contributors to Raman fluorescence consist of secondary minerals and any mixture where organics may be present [*Blacksberg* et al., 2014]. The "highly fluorescent" spectra from the mudstones examined in this work could potentially be associated with minor amounts of organic material that exhibits sharp peaks in the > 1650 cm^{-1} region and mixed in with other mineral phases that display shifts from 250-450 cm^{-1} as well as 1050 cm^{-1}. Lastly, the "undifferentiated" group represents areas that are very fine-grained interstitial fillings between framework grains with unidentifiable grain boundaries. Raman spectra returned from these areas generally exhibit low Raman intensities and consist of multiple components. In most cases, the spectra appear to be a mixture of at least three components and in most cases, up to five minerals contribute to low intensity Raman shifts. **Figure 12** represents the two most common microRaman spectral shapes in the undifferentiated group. The multicomponent spectra display peaks and a negative slope that are consistent with five mineral phases (biotite, muscovite, chlorite, quartz, and smectite). The proportion that each phase contributes to the overall spectrum cannot be determined in a straightforward manner. For this reason, the Raman spectra with multiple phases present are therefore classified as "undifferentiated". Future work to determine more accurate mineral abundances within the finest fraction should explore the capability of linear least squares models of Raman spectra.

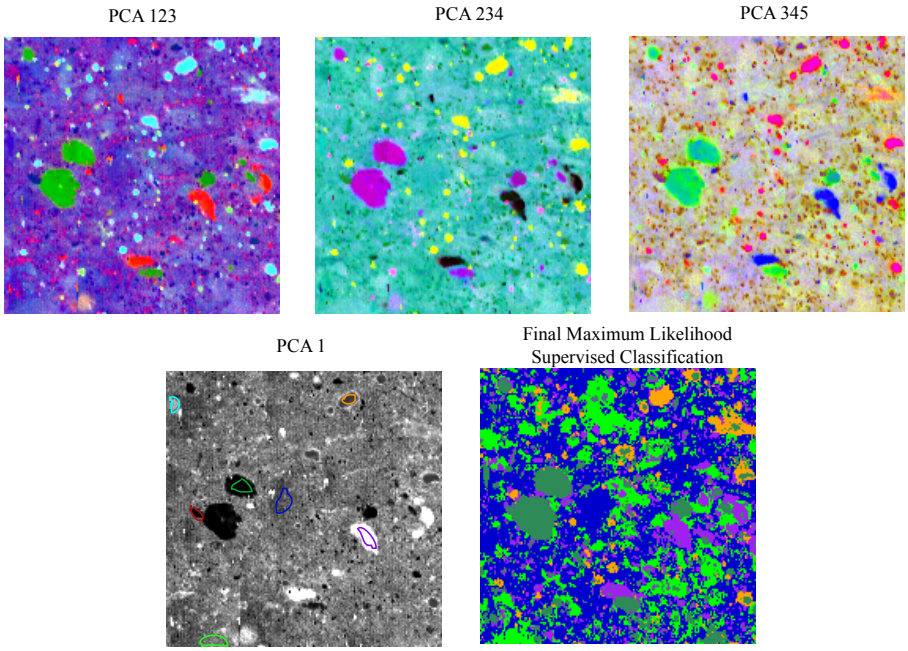

Figure 9. Principle component band combinations highlighting spectral variability within the microRaman scans. Regions of interest were selected from these band combinations and can be seen displayed in the bottom left image of PCA band 1. ROI's were then used to produced the final supervised classification image (bottom right).

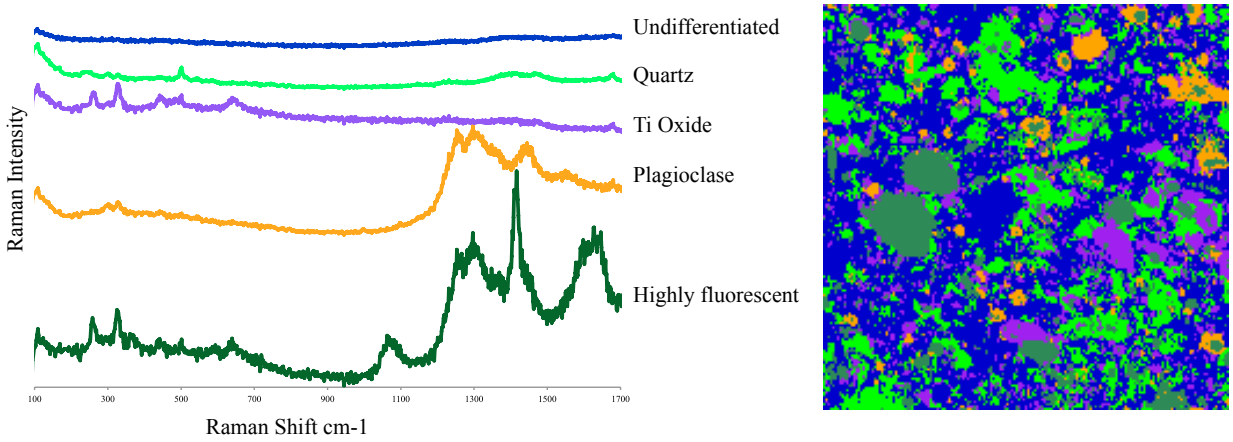

Figure 10. Example of a classification map with class mean spectra. (a) Spectra obtained from the microRaman point counts are displayed with (b) the coinciding classification picture produced from a 175 x 175 μm^2 grid scan using a maximum likelihood supervised classification. The color of the spectra match the classification colors used. Larger quartz, feldspar, and oxide grains are easily distinguishable from the more fine-grained undifferentiated class. The "highly fluorescent" spectrum, in comparison, produces fluorescence with high Raman peaks that mask any mineral phase identification below 1350 cm^{-1}.

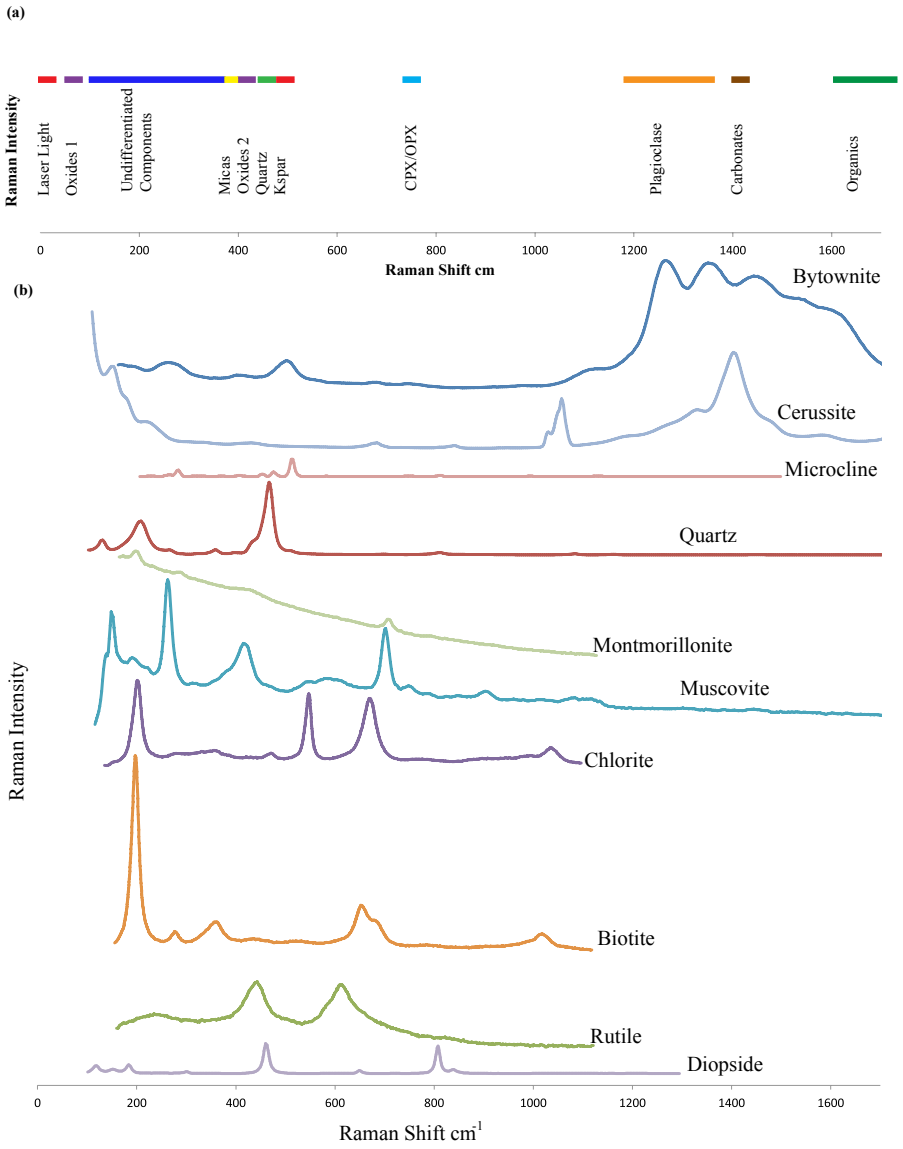

Figure 11. A schematic of the Raman shift locations of mineral phases that were identified from mudstone microRaman spectra (a). The most common microRaman library spectra that were used to identify phases in each mudstone spectrum are displayed (b) to serve as a reference for Raman shift location.

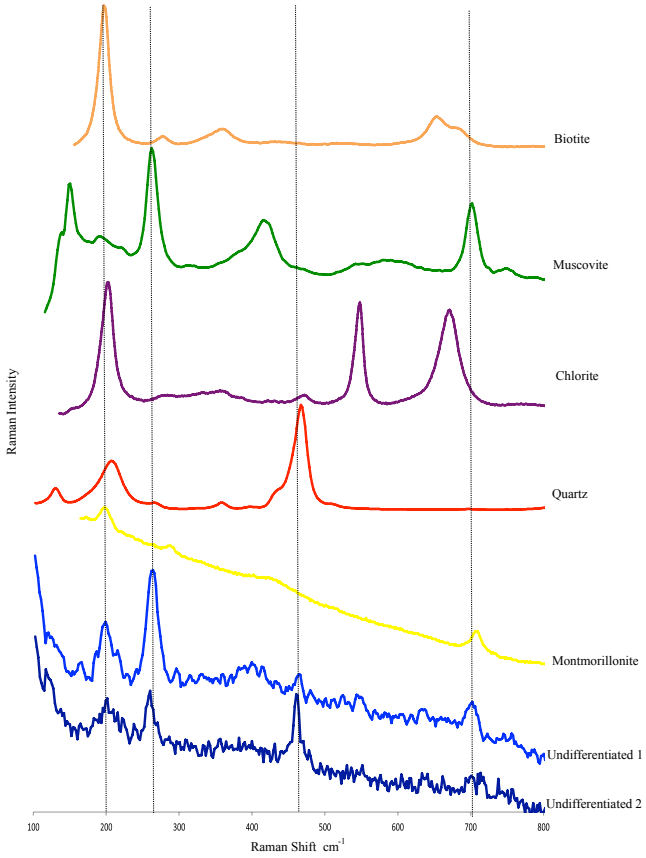

Figure 12. MicroRaman spectra from the very fine-grained interstitial fillings between framework grains in mudstones samples (the "undifferentiated" group) are compared with library Raman spectra of mineral phases that comprise the undifferentiated spectra. Two representative microRaman spectra from the undifferentiated group are displayed to illustrate the multiple components that contribute to the measured spectra. The undifferentiated group contains the same mineral phases and similar spectral shape, but exhibit distinct peak intensity differences that can be contributed to varying amounts of these phases.

4.5 Mudstone Classification

Compared to the bulk mineralogy of previously examined sandstones, mudstones contain less lithic fragments and a higher percentage of sheet silicates. For this reason, the same classification scheme cannot be applied. The mineral composition of the mudstones examined is displayed in the ternary diagram below (**Figure 13**). The relationship between total quartz and feldspar, clay and micas, and any other mineral phases present creates a generalized

classification scheme for comparison between the measured (circles) and model (same color, triangle), as well as the preliminary four XRD results (same color, square). The top corner represents detrital quartz and feldspar phases from both TIR and microRaman classifications. The "other" category in the bottom right corner includes the microRaman "highly fluorescent" and "oxide plus" class abundances as well as any other TIR mineral phases identified (carbonates, phosphates, sulfates, oxides, glass, and halides). The "clay + mica" corner of the triangle plot includes the undifferentiated group from microRaman and any sheet silicates and micas from the TIR models. This generalization for microRaman phase classification may result incorrect mineral abundance estimates because in mudstones, the same mineral phases (e.g. quartz) may be present in both the larger framework grains as well as the fine-grained matrix fraction. However, this ternary plot provides a cursory visualization of how rocks would be classified using each technique.

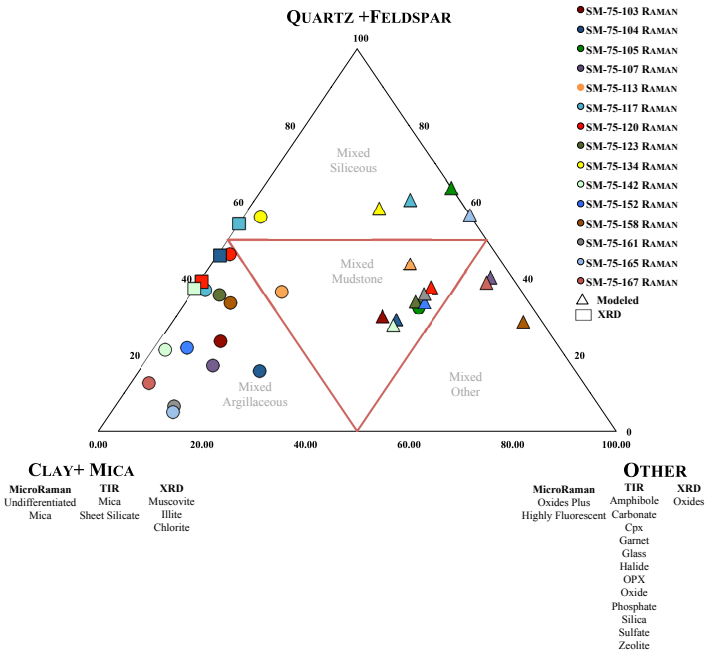

Figure 13. A mudstone classification scheme is depicted in the ternary plot comparing the results from microRaman point counts (circles), XRD (squares), and TIR models (triangles). MicroRaman and XRD

mudstone classifications are well correlated; whereas, TIR model classifications reflect more of a mixed composition mudstone.

For a more direct comparison, **Figure 14** is a scatter plot that relates the microRaman and TIR modal abundances for two groups: (1) quartz, feldspar, clay, and micas and (2) any other mineral phase present. This comparison does not distinguish between mineral clasts and the matrix or undifferentiated phases, allowing for total abundances to be accounted for. There is significant precision that is displayed in this technique comparison, with standard deviation within each specific group < 14 vol%, however the overall accuracy between techniques is rather poor.

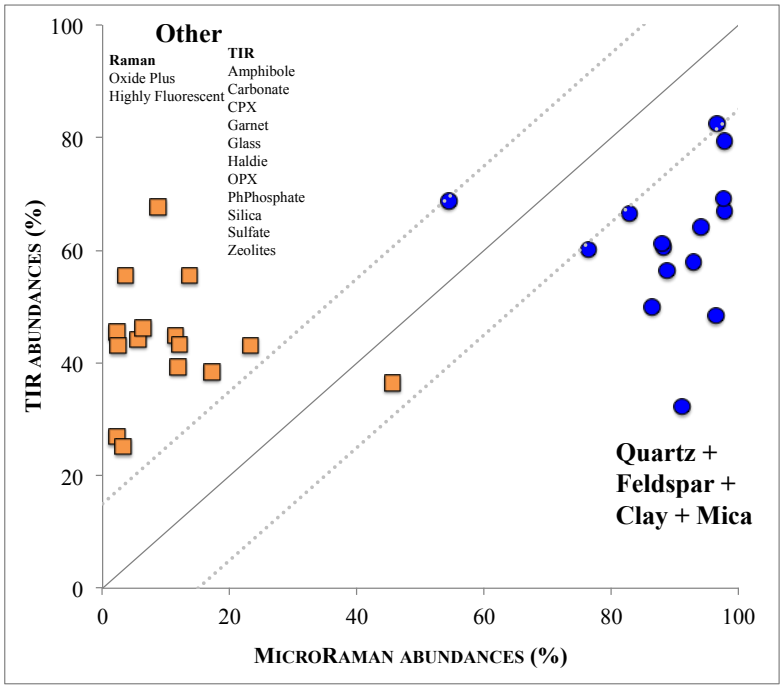

Figure 14. A scatterplot of microRaman abundances compared to TIR mudstone abundances. This figure excludes mineral clasts from matrix or undifferentiated phases and compares total mineral abundances. A perfect one-to-one relationship id depicted by the solid line and a ±15 vol% boundary is shown by the dotted lines.

4.6 QXRD subset

Mineralogy derived from microRaman results will serve as the "known" mineralogy of all mudstones examined in this work. However, for a subset of mudstones, mineral abundances were also derived using XRD techniques. Quantitative XRD results for four mudstone samples are displayed in **Table 7** as well as **Figure 15**. Abundances have been determined for only the well crystalline phases and normalized to 100%. Any amorphous, poorly crystalline, or organic component of these samples has not been identified, and thus the determined abundances from the Rietveld refinement are potential overestimates and should be considered relative to one another.

	SM-75-104 (G13)	**SM-75-120 (M4)**	**SM-75-117 (P4)**	**SM-75-142 (M8)**
Quartz	23.76	34.1	41.15	29.17
Plagioclase	22.21	5.05	13.07	8.15
Muscovite	41.26	47.05	31.54	50.33
Oxides (Hematite)	0.51	0.51	0	0
Chlorite	12.25	13.28	14.24	12.36
Goodness of fit (R^2)	8.13%	10.70%	8.99%	9.08%

Table 7. Quantitative X-ray diffraction results from a subset of mudstone samples

A plot of microRaman versus QXRD results (**Figure 15 a**) compares the two techniques and assesses the accuracy of Raman abundances as known mineralogy. All but two mineral abundances derived from the compared techniques had accuracies that were within ±15 vol% of each other. Overall, the microRaman determined abundances correlate well with the QXRD results, with an R^2 value of 0.84. Quartz displayed the strongest individual group relationship between the techniques ($R^2 = 0.60$), whereas plagioclase and "other" do not display as strong a correlation as quartz.

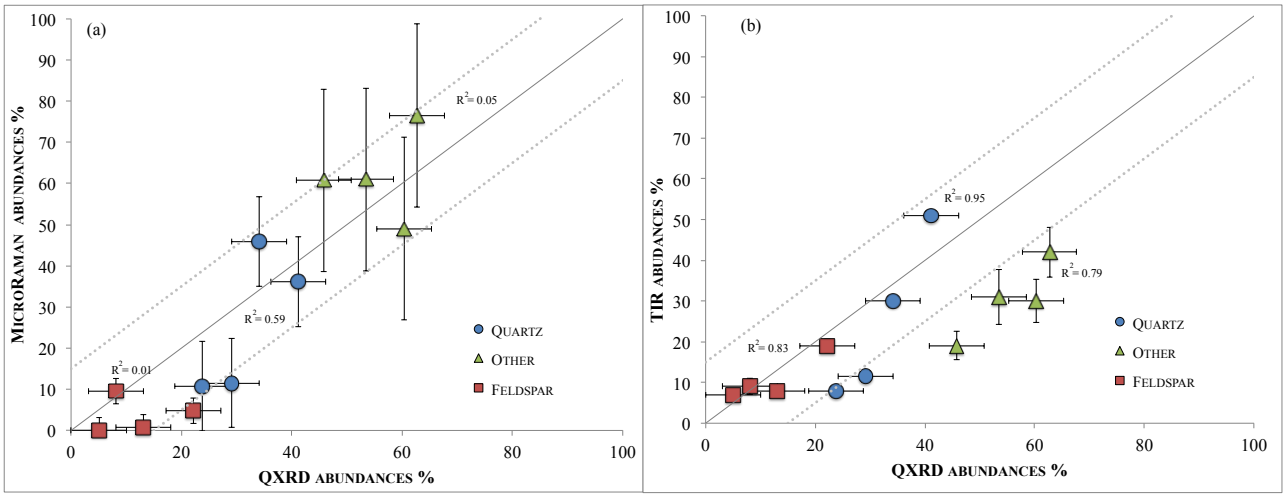

Figure 15. X-ray diffraction results are plotted against microRaman (a) and TIR derived abundances (b). Dotted lines are displayed to indicate a ±15 vol% from a one-to-one relationship (solid line). All but two points are confined within this limit for microRaman results. The highest average difference between the microRaman and QXRD is ±12.47 vol %. TIR results are less accurate for the "other" category, but individual mineral phases correlations are extremely good. Horizontal and vertical error bars display technique uncertainties (Section 4.8). Horizontal error bars are an average 5 vol % error for QXRD measurements. Vertical microRaman error bars are an average group error and the vertical TIR error bars are unique to each sample, as listed in Table 10.

In contrast to microRaman results, TIR models resulted in only ~58% of the derived abundances within ±15 vol% of the QXRD results (**Figure 15 b**). However, individual mineral phases had a stronger relationship between the techniques. Quartz, feldspar, and "other" measurements all correlated extremely well within their group, with corresponding R^2 values of 0.93, 0.83, and 0.79 (respectively).

A ratio of total quartz to the sum of total quartz + feldspar provides a direct comparison of all three techniques used for mudstone mineralogy (**Table 8**). The absolute difference between QXRD and TIR is 0.12 vol%, whereas the difference for QXRD and microRaman is 0.19 vol%. These results imply a stronger relationship between TIR and QXRD bulk abundances, and thus suggest that microRaman classification is underestimating total quartz abundances due to the presence of quartz within the "undifferentiated" spectra class.

Sample#	QXRD	TIR	microRaman
104	0.52	0.31	0.69
117	0.76	0.86	0.98
120	0.87	0.80	1.00
142	0.78	0.68	0.55

Table 8. QXRD ratio comparisons of quartz and the sum of quartz with feldspar.

4.7 Bulk Mineralogy (Measured vs. Modeled)

Sandstones

Modal mineralogy determined from petrologic point counts (known) are compared with spectrally derived (modeled) abundances for each sandstone (**Figure 16**). The average differences between the measured and the modeled abundances as well as the one-sigma standard deviation of the absolute differences are presented in **Table 9**. Quartz displays the lowest mean difference (3.81 vol %) and standard deviation (± 3.24 vol %), which coincides with the relatively perfect linear fit. Both feldspar and "other" also display strong correlations with average differences of 4.81 ± 5.14 vol % and 9.39 ± 7.23 %. These sandstone absolute differences and uncertainties fall within the accuracy associated with traditional point counting techniques (± 5-15 vol %), which also compares well with previous work done by *Feely and Christensen*, [1999].

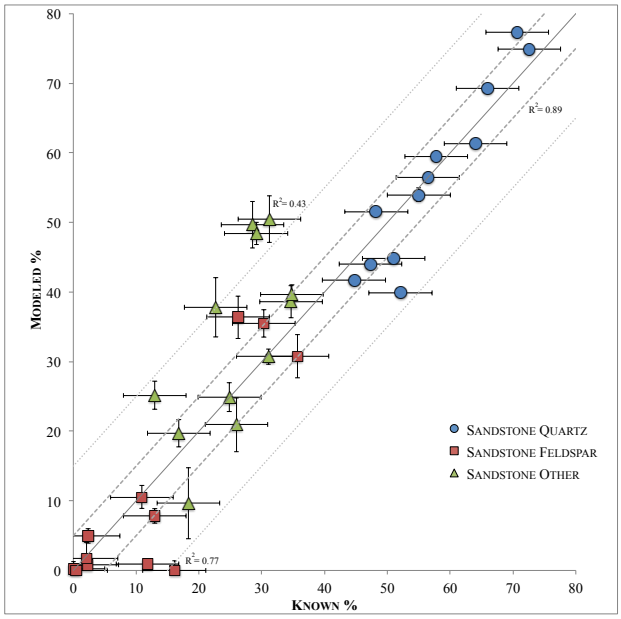

Figure 16. A scatterplot of the mineral abundances for sandstones determined from traditional point counts (known) versus modeled mineral abundances derived from unmixing TIR spectra (modeled) displays an extremely good fit. The solid line indicates a one-to-one relationship between the models; where as, a lighter dotted lined signifies a ±15 vol% boundary, and a darker dotted line confines a ±5 vol% difference. The triangular shaped "other" class contains all minerals that were not identified as a quartz or feldspar clasts. A relatively linear mixing correlation between the two techniques can be concluded from this plot. Technique uncertainties are displayed by the error bars and are unique to each sample for TIR models (**Table 10**) and are averaged for point counts at 5 vol %.

In addition to calculating accuracy, I also calculated the individual correlation value within each mineral group as well as evaluated the overall linear correlation between traditional point counting and TIR techniques. The two techniques correlate well, with an overall R^2 value of 0.86. Quartz displays the strongest group correlation (R^2 = 0.89) with many samples overlapping the line of a perfect linear match. Feldspar (R^2 = 0.77) also shows a strong correction with all but one measurement falls within ± 15% of the known value. The class containing all other phases has a more scattered pattern with a correlation of R^2 = 0.43 and three samples falling just outside the ± 15% range.

	Sandstones Mean ± 1 σ Difference (%)	Mudstones Mean ± 1 σ Difference (%)	Sandstones Median Difference (%)	Mudstones Median Difference (%)
Quartz	3.8 ± 3.2	10.0 ± 7.2	3.1	7.3
Feldspar	4.8 ± 5.1	19.7 ± 12.6	3.7	18.3
Other	9.4 ± 7.2	13.1 ± 9.3	6.8	9.9

Table 9. Comparison of the known and modeled mineral abundances of both sandstones and mudstones. Mean differences are calculated from the absolute differences in mineral abundances, shown in Figures. 16 and 17.

Mudstones

Figure 17 displays the comparison between the bulk mineralogy determined from microRaman scans and the mineral abundances derived for TIR spectral deconvolution. For mudstones, quartz displays the lowest average absolute difference (10.0 ± 7.2 vol%) between the measured and modeled abundances (**Table 9**). Feldspars exhibits the highest mean difference (19.7 ± 12.6 vol%). The "other" class has an intermediate average difference of 13.1 ± 9.3 vol%.

Although to a lesser degree than sandstones, the overall correlation between the two techniques for mudstones still shows a relatively strong fit ($R^2 = 0.61$). Quartz is the most well correlated mineral phase group with an R^2 value of 0.55. Measurements within feldspar and "other" groups display a more scattered distribution, with reasons for potential incoherence between techniques discussed in sections to follow. However, all but three measurements for other fall within ± 15 vol % of the accepted value whereas less than half of feldspar measurements meet this criterion.

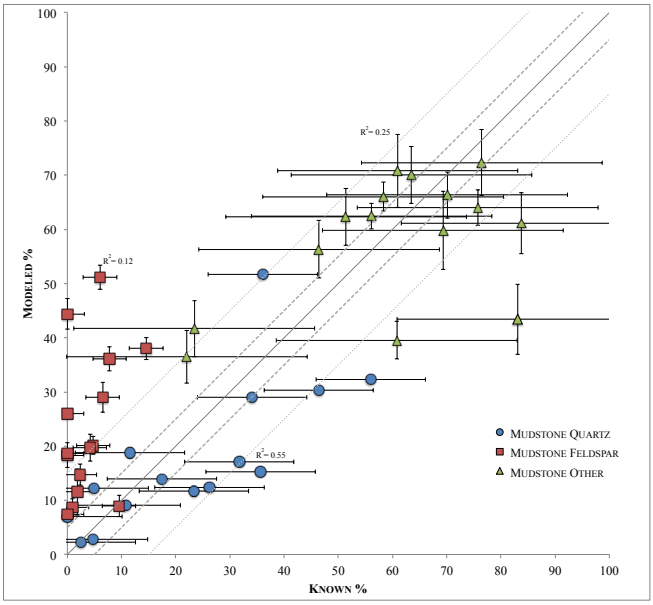

Figure 17. A scatterplot of the mineral abundances for mudstones determined from microRaman point counts (known) versus modeled TIR abundances. The three boundaries consist of a perfect fit (solid line), a ± 5 vol % difference (darker dotted line), and a ± 15 vol % difference (lighter dotted line). Technique uncertainties are displayed by the error bars are unique to each sample for TIR errors and averaged for microRaman errors (**Table 10**).

4.8 Technique Uncertainties

All techniques employed in this study are subject to technique uncertainties that are displayed in **Table 10** and as error bars in **Figure 16** and **17**. The uncertainties given for the TIR models are standard errors of coefficients from the least squares minimization routine [*Rogers and Aharonson*, 2008]. The numerical errors are dependent on the other phase abundances returned from the model, but do not account for systematic errors associated with missing endmembers, inaccurate particle size of endmembers, or nonlinear mixing associated with smaller grain sizes. Assessment of those uncertainties comes from the comparison with other techniques (Section 5). In general the standard error is low, between 0.57 and 6.76 vol % (**Table 10**). The uncertainties related to microRaman point counts are estimated by calculating the absolute difference between the two classifications done on the same rock sample (Section

3.2.4). The uncertainties associated with this technique range from 0.07 to 51.47 vol % (**Table 10**). The implications of this will be discussed in further detail in Section 5.3. Traditional point count uncertainties are evaluated by the number of total points counted as well as the reproducibility of conducting multiple counts on the same thin section. With an average of ~250 point counted per thin section, the uncertainty associated with the traditional modal mineralogy estimates ranged from < 5 vol % to 10 vol %. X-ray diffraction errors are generally low and are associated with the quantitative analysis technique employed. For major crystalline phases that make up more than 10 vol % of the sample analyzed, the uncertainty is generally < 5 vol % [*Środon et al.*, 2001].

a		*Quartz*	*Feldspar*	*Other*
SM-75-103	*TIR*	0.93	2.25	5.23
	Raman	23.41	-	25.28
SM-75-104	*TIR*	0.82	1.67	6.76
	Raman	15.27	0.64	19.90
SM-75-105	*TIR*	0.72	2.23	4.86
	Raman	2.67	8.56	48.37
SM-75-107	*TIR*	0.74	2.02	7.21
	Raman	3.52	8.82	8.88
SM-75-113	*TIR*	0.70	1.91	5.31
	Raman	15.56	3.32	11.48
SM-75-117	*TIR*	0.50	1.47	3.51
	Raman	14.36	0.57	10.94
SM-75-120	*TIR*	0.62	0.77	5.27
	Raman	11.48	0.00	51.47
SM-75-123	*TIR*	0.70	0.00	2.64
	Raman	7.78	-	8.54
SM-75-134	*TIR*	0.50	0.70	5.20
	Raman	1.98	-	34.74
SM-75-142	*TIR*	0.95	1.95	6.11
	Raman	3.04	13.52	16.82
SM-75-152	*TIR*	0.61	2.45	4.23
	Raman	6.43	5.09	8.00
SM-75-158	*TIR*	0.47	4.23	2.37
	Raman	44.83	2.11	45.11
SM-75-161	*TIR*	0.63	2.77	3.24
	Raman	-	3.43	21.16
SM-75-165	*TIR*	0.57	2.85	6.44
	Raman	6.93	0.07	12.25
SM-75-167	*TIR*	0.56	2.23	5.60
	Raman	6.72	0.23	10.34
Average	***TIR***	**0.67**	**1.97**	**4.93**
Average	***Raman***	**10.09**	**3.09**	**22.22**

b	16.606	La Boca	Mis-Te-2	Tx-Te-1	Devil K	D1-72-91	Catskil Sk-1	Smithwick	Flat Irons	Bera	Gratton	Mt. Tom
	TIR	*TIR*	*TIR*	*TIR*	*TIR*	*TIR*	*TIR*	*TIR*	*TIR*	*TIR*	*TIR*	*TIR*
Quartz	0.50	0.45	0.27	0.47	0.42	0.99	0.63	0.53	0.47	0.53	0.42	0.41
Feldspar	1.02	1.08	0.42	1.63	1.03	3.04	0.61	2.31	1.94	0.00	1.38	3.12
Other	2.31	3.34	1.36	3.34	2.07	5.13	4.25	3.88	1.97	1.10	1.60	2.00

Table 10. Uncertainties for microRaman derived abundances (a) and sandstone TIR models (b). Traditional point counts and QXRD are not displayed and are generally low ranging from < 5 to 10 vol % for point counts and < 5 vol % for major crystalline phase in QXRD.

5. Discussion

Thermal emission spectral models have produced results consistent with other commonly used techniques for quantifying mineral abundances. The findings from this investigation can be broken down into effectiveness of TIR spectroscopy at identifying individual mineral phases as well as the usefulness of TIR spectroscopy at classifying the bulk mineralogy of sand sized or smaller grained sedimentary rocks. Implications from this work along with recommendations for future investigations are addressed in this section.

5.1 Mineral Phase Identification

The analyses of sandstones by TIR spectroscopy revealed a composition primarily composed of quartz, both plagioclase and alkali feldspars, micas, and clay mineral phases. In comparison, mudstone spectral unmixing produced bulk rock compositions mainly composed of quartz, plagioclase, and clay mineral phases. Qualitatively, these results are consistent with typical sedimentary rock compositions. But the efficiency in identifying individual phases is determined through comparison with other techniques.

Quartz was readily identified from TIR spectra of both mudstones and sandstones. As expected in a typical sedimentary rock composition, both detrital granular quartz as well as

microcrystalline phases were identified. These results are consistent with the optical properties (texture) that were examined under the petrologic microscope.

Feldspars in sedimentary rocks can be diagenetically altered, thus making identification by various techniques a challenging task. TIR has proven to be a viable technique for feldspar identification, with previous studies determining average plagioclase composition in complex sand mixtures of varying plagioclase series members to within 6% An content [*Milam et al.*, 2007] and total feldspar can be detected in bulk rock spectra with at least 5% abundances within 4 vol % accuracy of the known composition [*Hecker et al.*, 2010]. In this study, plagioclase is the dominant feldspar in the TIR spectra of mudstones examined, with albite, bytownite, and oligoclase being the most commonly modeled phases. These results agree with the findings from microRaman and QXRD analyses, which showed evidence for both albite, oligoclase, and bytownite. Additionally, previous geochemical and petrographic analysis of Huronian mudstones suggests that sodium metasomatism in the form of albitization was widespread within this formation [*Fedo et al*., 1997]. Although *Fedo et al*., 1997 determined complete albitization occurred, results from TIR, QXRD, and microRaman suggest minor amounts of other *An-Ab* solid solution endmembers present within these mudstones.

Sandstone TIR results returned feldspar content consistent with mainly albite, microcline, and labradorite. These mineral phases agree with the common optical properties examined in thin section that differentiates the two feldspar phenocryst as well as previous work addressing the success of TIR modeling in identifying feldspar [*Hecker et al.*, 2010]. For example, sandstone samples Flat Irons and Tx-Te-1 display obvious differences in feldspar phase contributions in both photomicrographs (**Figure 6**) as well as the TIR spectrally derived abundances (**Figure 5**).

Clay mineral phase identification by thermal emission spectroscopy is sensitive to the interlayer configuration of cations as well as the Si/O stretching ratio that occurs in the frequency range of ~1300-950 cm^{-1}. The advantage of using TIR spectroscopy for clay identification is the limited sample preparation required compared to other techniques. Previous work by *Michalski* et al., [2006], determined that the mineralogical variations among clay minerals can be observable in the TIR spectral range leading to accurately estimated clay abundances, but emitted photons can also interact with multiple phases and thus produce incorrect individual phase identification. In this study, TIR spectral models of sandstones commonly identified kaolinite and montmorillonite, which agrees with initial petrologic assessment of the clay matrix's textural features. However, in some samples that displayed clay/mica-rich abundances from optical point counts, sheet silicate library spectra were not modeled from the TIR unmixing algorithm. For example, the matrix of sample Mt. Tom, which accounted for ~13 vol%, was qualitatively described as an iron-rich micaeous clay. The TIR model returned no identification of clay. The nonlinear mixing of mudstone mineral phases may partially arise from a gap in our spectral libraries that includes diagenetically altered phases (sericite). With mineralogical data returned from the MSL *Curiosity* rover at Yellowknife Bay identifying mudstones with phyllosilicate content of 28-31 wt% [*Vaniman et al*., 2014], the addition of more clay phases to the thermal emission spectral library will greatly increase the ability of TIR spectroscopy in deriving bulk mineralogy.

Furthermore, mudstone clay identification was inconsistent with results from XRD and microRaman results. Generally, XRD results determined illite group members to be the dominant clay phases. MicroRaman results identified both illite and smectite group members based on peak location and spectral slope, but were unable to determine the percentage that each clay

phase contributed to the undifferentiated spectra. However, TIR models mainly identified smectites, in particular palygorskite (Palygorskite solid PR1-1) as the only clay contributing to mudstone spectra. The discrepancy in the clay phase identification can be the result of intrinsic flaws that exist in all techniques employed. The QXRD results are relative and only identify the well crystalline material in our samples; therefore any poorly crystalline clay, in this case smectites, may be under estimated. MicroRaman results may be distorted by the high fluorescence of organics potentially associated with clays and thus overpowering individual spectrum identification of these phases. Similarly, the extremely fine crystal size of clay minerals allows for emitted energy to interact with a variety of phases and consequently, an inconclusive identification from the unmixing of its TIR spectra is observed. Also contributing to inaccuracies in TIR models may be poorly characterized reference materials; some clay phases may be impure and contain mica phases. Thus we conclude that sheet silicate mineral identification in sedimentary rocks suffers inherent inaccuracies associated with all techniques examined.

TIR spectra for three mudstones and one sandstone display an obvious carbonate contribution, determined from the frequency range of ~1600-1500 cm^{-1}; however, for these same examples, microRaman and traditional optical point counts failed to detect carbonate phases. This presents a case where thermal emission spectroscopy exceeds the accuracy of the other techniques employed in this study. Carbonate phases have very distinct features in the TIR and have been previously examined in TIR laboratory work that resulted in accuracies within 3-5% of known carbonate series identification from a suite of 29 carbonate bearing samples [*Lane and Christensen*, 1997]. The TIR capability of detecting carbonate directs the attention to the other technique limitations. Optical point counts qualitatively address the matrix components and could potentially over overlook carbonate contributions, whereas, microRaman results may be

limited from non-representative portions of the samples. MicroRaman spectra may also suffer from highly fluorescent phases coating authigenic carbonate series members, which will result in a spectrum that overwhelms the incident laser light and thus leading to potential inaccurate carbonate abundances.

Lastly, TIR spectral models identified "glass" phases in 12 out of the 15 mudstones examined. In the TIR, obsidian glass features are indistinguishable from opaline silica and poorly crystalline phases [*Kraft et al*., 2003], which may be present within in our samples. However, microRaman and XRD techniques failed to recognize this component of mudstone samples due to instrument and method limitations. The XRD method employed here did not calculate an amorphous component and microRaman spectroscopy of poorly crystalline materials is difficult to obtain [*Frost*, 1997] with the intensity and duration of a large scan used for this classification technique.

5.2 Mineral Abundance Quantification

Overall mineral abundances determined from the unmixing of thermal emission spectra of sandstones are in relatively good agreement in comparison to traditional point counts, with measurement accuracies within 5 vol % for framework minerals and within 10 vol % for matrix components. Traditional point counts returned an average sandstone composition of 57.2 vol % quartz, 6.9 vol % plagioclase, 5.7 vol % alkali feldspar, and 25.9 vol % matrix material (all other abundances were <5 vol %). In comparison, TIR model derived abundances returned an average sandstone composition consisting of 56.2 vol % quartz, 7.2 vol % plagioclase, 3.6 vol % alkali feldspar, and 33.0 vol % potential matrix components. Although comparison of matrix material assessed by optical petrologic techniques to TIR derived group abundances is not direct, a priori

knowledge of potential matrix components allows for relationships between the techniques to be assessed. Therefore, TIR mineral abundances of micas, clays, carbonates and all other groups that were not quartz or feldspar were combined to serve as the matrix ("other" category in the linear/ternary plots) for comparisons to the traditional point count modal abundances. This resulted in a > 92 % agreement between model results and traditional point count results within ± 15 vol % of the point count abundances (**Figure 15**). Furthermore, ~69% of the derived abundances for sandstones were within ±5% the known value. Individual group examination resulted in 75 % of quartz and feldspar abundances as well as > 50 % of the potential matrix components to be molded within ± 5 vol % the point count values.

In contrast, mineral abundances from TIR spectral models of mudstones show larger differences (< 10 vol % for quartz, < 19.7 vol % for feldspars, and < 13.1 vol % for all other components) from the technique used to provide known mineralogy (microRaman). Mudstone bulk mineralogy determined from microRaman point counts resulted in an average mudstone composition of 22.8 vol % quartz, 3.9 vol % plagioclases, 1.8 vol % micas, 6.1 vol % a highly fluorescent component, and 60.1 vol % of an undifferentiated matrix material consisting of mica, biotite, quartz, and chlorite (all other abundances were < 5 vol %). Comparatively, TIR derived abundances returned an average mudstone composition of 17.7 vol % quartz, 23.0 vol % plagioclase, 5.7 vol % mica, and 53.6 vol % of all other potential matrix components. For mudstones, greater than 66 vol % of the mudstone modeled mineral groups fell within ± 15 vol % of the microRaman results (**Figure 17**). In addition to bulk comparisons, individual groups returned 80 % of quartz, 46 % of feldspars, and 73 % of "other" phases within ± 15 vol % the microRaman point count results.

Further exploration of sandstone and mudstone compositions reverted to traditional ternary classification plots, showed that ~66 % of the sandstones but only ~13 % of the mudstones modeled were within the same classification scheme as their co-analyzed techniques (**Figure 7** and **13**). For sandstones, misfits between the measured and modeled composition as well as classification are relatively insignificant but can be addressed with a few different potential reasons. Three out of the four misfits can be attributed to the TIR models containing less feldspar than the traditional point count estimates. The reason for this discrepancy can be the difficulty for both techniques in discerning between diagenetically altered feldspar and clay. Traditional point counts may have noted a degree of alteration along the rim of a feldspar grain and still classified the grain as feldspar, whereas TIR spectroscopy with a sample penetrating depth on the order of $\sim 10^0$-10^1 μm (using the Beer-Lambert Law) may have inheritably acquired spectral features of sheet silicates. Another source of ambiguity stems from the generalization of the TIR potential matrix components (necessitated for comparison to the optically derived modes). The matrix may also contain quartz and feldspar phases, which in turn will lead to inadequate estimates for both clasts and matrix contributions from these phases. This assumption allowed for comparisons between the techniques but also produced the least correlated group examined (R^2=0.43).

Mudstone discrepancies are more apparent and warrant a more in depth exploration of technique limitations. The majority of mudstones examined by microRaman point counts returned classifications of clay dominated or mixed argillaceous mudstone, which coincided with three out of the four XRD classifications. However, the common classification derived from the TIR models was a mixed mudstone (**Figure 13**). The source of inconsistency in mudstone classification is the result of the intrinsic error of both techniques. First, the microRaman scan

areas were limited to 61,250 μm^2. Although mudstone samples are generally homogenous compared to other sedimentary rock types, the accuracy of microRaman results may be affected by the small areas sampled (**Table 10**). Secondly, both techniques have a difficult time accounting for any potential organics mixed or coating mineral components.

Organics (> 1650 cm^{-1}) result in high fluorescence within a microRaman spectrum that overwhelms the spectrum across the entire range. This results in a highly non-linear contribution of organics to the microRaman spectrum that potentially does not correspond to the true abundance. Also, fine particulates can result in scattering as well as reduced feature contrast, leading to model abundance inaccuracies. However, these Archean mudstones have been previously analyzed for total carbon content and the majority of samples returned compositions with little carbon [*Cameron and Garrels*., 1980]. Thus, any minor amount of organic content may have dramatic effects on microRaman and potentially TIR abundances.

Another source of error may result from quartz phases being present as both detrital grains as well as undifferentiated matrix components in the Raman classification (**Figure 12**). Similarly to sandstones, this may lead to overestimates of quartz and underestimates of matrix contributions in the microRaman derived abundances. This idea is supported by the scatter plot (**Figure 14**) that evaluates total mineral phase abundances in the mudstone samples by taking into account any quartz or feldspar present in the matrix or undifferentiated components. Generally, this comparison tends to show a stronger correlation between the groups compared but produces less accurate abundance estimates with an average difference of ~30 vol % and a standard deviation below ± 15 vol %. This idea is also supported by **Table 8**, which shows similar quartz/feldspar proportions between the TIR and QXRD. Because both of these techniques are insensitive to where the quartz is manifested in the samples (mineral clasts vs.

matrix), the similar proportions of crystalline components suggest that microRaman may be underestimating quartz abundances.

Fourth, the modeled glass component in the TIR, which likely represents poorly crystalline aluminosilicates or opaline silica, cannot be accounted for in the Raman or QXRD analyses used, resulting in a mismatch between classifications, with TIR-based classifications shifted towards the "other" corner, and into the "mixed argillaceous" category.

Lastly, clay minerals, clay aggregates, and matrix sized material (<30 μm) produces a volume scattering effect in the TIR spectra [*Ramsey and Christensen*, 1998]. The emitted photons from this intimate, finely grained clay fraction of both mudstones and sandstones interacts with multiple phases before being detected and therefore making individual clay phases less distinguishable in TIR spectroscopy, when intimately mixed.

From the evaluation of thermal emission spectroscopy of sedimentary rocks, we conclude that the linear unmixing technique employed here is a very suitable candidate for deriving mineral abundances, however we recognize the limitations in discerning individual components that comprise the matrix fraction of sandstones and mudstones. Well crystalline framework minerals in sandstones are readily identified with correct phases and abundances are modeled within < 5 ± 5 vol % the accepted value. More heavily altered framework grains within mudstones samples are still correctly identified but suffer a larger average error in modeled abundances (quartz = 10.0 vol % and feldspar = 19.7 vol %). Although derived mineral abundances are within a suitable error for most mineral groups (except mudstone feldspar mean difference = 19.7 vol %), accurate identification of individual mineral phases within the less than <30μm fraction of both sample sets remains challenging.

5.3 Evaluating Technique Uncertainties

The inherent uncertainties associated with each technique employed is fundamental to consider when evaluating measurement accuracies. Although there is discrepancy in the quantification of the matrix components for traditional point counts and the poorly crystalline fraction of QXRD abundances, the overall reproducibility of these techniques is consistent. Uncertainties associated with TIR are models are controlled by a number of factors, that for this study mainly include the number of library spectra used in the models, the library containing all correct mineral phases present in the sample, and the overall complexity of the sample itself [*Rogers and Aharonson*, 2008]. Even after grouping the mineral phases for comparison (**Figures 16** and **17**), the propagation of uncertainties within this technique remains relatively low (in comparison to other techniques used). Similarly, the errors associated with traditional point counts and QXRD are also generally low. However, the classification techniques used for the microRaman point counts showed high variability for some samples. For example, mudstone sample SM-75-120 displayed a 51 vol % difference between the two scans for the "other" class (**Table 9**). These higher uncertainties are a function of sample heterogeneity and insufficient sampling size, and thus the true uncertainties associated with TIR models may be lower.

5.4 Implications for Terrestrial and Martian Sedimentary Rocks

The combination of mineralogy results from thermal emission unmixing investigations of igneous and metamorphic rocks [*Feely and Christensen*, 1999] , mafic rocks [*Hamilton and Christensen*, 2000], and basaltic rocks [*Wyatt et al.*, 2001] with the findings from the work presented here, makes TIR spectroscopy an advantageous resource for both earth based and planetary bound studies. Though our ability to confidently identify all mineral phases within the

matrix and clay sized fraction remains inconclusive among techniques examined, the ability to distinguish bulk mineralogy demonstrates the effectiveness of thermal emission spectroscopy in characterizing sedimentary rocks.

Although limitations exist in the complete mineralogical identification and quantification of sedimentary rocks by TIR spectroscopy, the compelling reasons to utilize this technique outweighs others techniques examined in this work. The acquisition of TIR spectra (approximately 8 minutes) is extremely rapid in comparison to XRD, microRaman point counts, and traditional point counting techniques. Also TIR spectroscopy is a non-destructive technique, which may serve as a valuable resource when discussing future sample return missions. Overall, TIR spectroscopy can return mineralogical abundances within ± 3.8-19.7 vol% the accepted value for sedimentary rocks and serve as a rapid, first means identification tool.

6. Conclusion

Thermal infrared spectral unmixing of laboratory-acquired spectra has been examined for its effectiveness in deriving modal mineralogy of sandstone and mudstone sedimentary rocks. A suite of sandstones and mudstones spanning a wide range of composition, compaction, grain size, alteration, and texture were investigated by multiple techniques designed to provide an in depth analysis of the advantages as well as limitations of TIR spectroscopy. Common sandstone composition (as determined by traditional point counts) consisted of quartz, feldspars, micas, clays, and a matrix/cement component unique to each sample; whereas, mudstone composition (as determined by XRD and microRaman) typically was comprised of quartz, plagioclase, and an abundant amount of a dynamic clay sized multi-component mineral mixture. Derived mineralogy from TIR spectra are highly correlated with these results; however, larger mineral clasts display

a more conservative linear mixing behavior in comparison to mineral phases that make up the more fine-grained matrix component.

The mineralogical results of this work provide TIR bulk rock abundances that are within 10 vol % for sandstones and within 20 vol % for mudstones, in comparison to the other techniques investigated. The identification of mineral phases that contribute to the < 30 μm grain size fraction remains highly ambiguous among the techniques examined, with each technique constrained by its own intrinsic limitations. Traditional petrographic analysis of thin sections produces accurate estimates of mineral clasts but can only qualitatively assess the content in the matrix fraction. MicroRaman analysis is limited by highly fluorescent phases, small sampling areas, and also the present lack of laboratory work demonstrating linear contributions in multi-component spectra. X-ray diffraction requires extended sample preparation in order to identify non-crystalline (or poorly crystalline) phases that may be present in the matrix. TIR spectral modeling is affected by fine-grained, intimate mixtures in which photons emitted interact with multiple phases and can therefore result in reduced accuracy of individual mineral phase abundance estimates.

The close investigation of the individual uncertainties associated with multiple techniques in determining bulk mineralogy demonstrates the utility that thermal emission spectroscopy can have in both a terrestrial as well as planetary setting. The wide spread occurrence of sedimentary rocks on the Martian surface is the foundation for enhancing our ability to remotely identify sedimentary mineralogy. Thermal emission spectroscopy has the ability to provide a rapid and also nondestructive first order analysis of samples, with accuracies consistent with the other techniques examined. Such analysis will guide further sample investigations (geochemistry,

geomorphology, and geochronology) as well as provide a framework for potential sample return missions.

7. Future Work

While this thesis has demonstrated the utility of using TIR spectroscopy for characterizing the mineralogy of sandstones and mudstones, further development will continue to place better constraints on the uncertainties and overall mixing linearity of sedimentary rocks. This work will be enhanced in a number of ways, including: re-quantifying XRD abundances in order to account for poorly crystalline or amorphous phases, adding more clay endmembers to the spectral library, examining microRaman classes at an increased magnification, and continually expanding the amount of natural samples examined. These recommendations will help in accomplishing the overarching goal aimed at improving our interpretations of remotely sensed data.

Each future recommendation will specifically address areas that can expand our knowledge from the foundation of this thesis. First, identifying absolute abundances from XRD profiles will provide a more direct comparison for bulk rock measurements between TIR models and XRD results. Next, the addition of more phyllosilicate phases to our spectral library from phases previously analyzed in work by *Che and Glotch* [2012], will allow for a more accurate determination of clay phases. Thirdly, increasing the magnification used for microRaman classifications from 50 X to 100 X may reveal more distinct Raman shifts for the low intensity "undifferentiated" class. Lastly, including additional sedimentary rock samples will provide further justification for this technique by incorporating even more variability among samples.

References

Baldridge, A., J. Farmer, and J. Moersch (2004), Mars remote-sensing analog studies in the Badwater Basin, Death Valley, California, *Journal of Geophysical Research-Planets*, *109*(E12), doi:10.1029/2004JE002315.

Baldridge, A.M., (2008). Thermal emission studies of sulfates and chlorides: Implications for salts on the martian surface. PhD dissertation, Arizona State University, Tempe

Bandfield, J. (2008), High-silica deposits of an aqueous origin in western Hellas Basin, Mars, *Geophysical Research Letters*, *35*(12), doi:10.1029/2008GL033807.

Bandfield, J., V. Hamilton, and P. Christensen (2000), A global view of Martian surface compositions from MGS-TES, *Science*, *287*(5458), 1626-1630, doi:10.1126/science.287.5458.1626.

Bergmann, J., P. Friedel, and R. Kleeberg (1998), BGMN-a new fundamental parameters based on Rietveld program for laboratory X-ray sources, it's use in quantitative analysis and structure investigations, Commission of Powder Diffration, International Union of Crystallography CPD Newslett. 20 5-8

Bibring, J., et al. (2006), Global mineralogical and aqueous mars history derived from OMEGA/Mars express data, *Science*, *312*(5772), 400-404, doi:10.1126/science.1122659.

Blacksberg, J., et al. (2014), Time-Resolved Raman Spectroscopy for Planetary Science, *11th International GeoRaman Conference* (5055), St. Louis, Missourri

Blatt, H., R. J. Tracy, and B. E. Owens (2006), *Petrology Igneous, Sedimentary, and Metamorphic* 3rd ed., W.H. Freeman and Company, New York.

Cameron, E., and R. Garrels (1980), Geochemical compositions of some Precambrian shales from the Canadian Shield, *Chemical Geology, 28*(3-4), 1810197, doi:10.1016/0009-2541(80)90046-7.

Che, C., and T. Glotch (2012), The effect of high temperatures on the mid-to-far-infrared emission and near-infrared reflectance spectra of phyllosilicates and natural zeolites: Implications for martian exploration, *Icarus*, *218*(1), 585-601, doi:10.1016/j.icarus.2012.01.005.

Christensen, P., J. Bandfield, V. Hamilton, D. Howard, M. Lane, J. Piatek, S. Ruff, and W. Stefanov (2000), A thermal emission spectral library of rock-forming minerals, *Journal of Geophysical Research-Planets*, *105*(E4), 9735-9739, doi:10.1029/1998JE000624.

Christensen, P., et al. (2001), Mars Global Surveyor Thermal Emission Spectrometer experiment: Investigation description and surface science results, *Journal of Geophysical Research-Planets*, *106*(E10), 23823-23871, doi:10.1029/2000JE001370.

Ehlmann, B. L., D. L. Bish, S. W. Ruff, and J. F. Mustard (2011), Mineralogy and chemistry of altered Icelandic basalts: Application to clay mineral detection and understanding aqueous environments on Mars, *Journal of Geophysical Research*, *117*(E00J16), doi:10.1029/2012JE004156.

Fedo, C., G. Young, H. Nesbitt, and J. Hanchar (1997), Potassic and sodic metasomatism in the Southern Province of the Canadian Shield: Evidence from the Paleoproterozoic Serpent Formation, Huronian Supergroup, Canada, *Precambrian Research*, *84*(1-2), 17-36, doi:10.1016/S0301-9268(96)00058-7.

Feely, K., and P. Christensen (1999), Quantitative compositional analysis using thermal emission spectroscopy: Application to igneous and metamorphic rocks, *Journal of Geophysical Research-Planets*, *104*(E10), 24195-24210, doi:10.1029/1999JE001034.

Frost, R. (1997), The structure of the kaolinite minerals - a FT-Raman study, *Clay Minerals*, *32*(1), 65-77, doi:10.1180/claymin.1997.032.1.08.

Glotch, T., J. Bandfield, P. Christensen, W. Calvin, S. McLennan, B. Clark, A. Rogers, and S. Squyres (2006), Mineralogy of the light-toned outcrop at Meridiani Planum as seen by the Miniature Thermal Emission Spectrometer and implications for its formation, *Journal of Geophysical Research-Planets*, *111*(E12), doi:10.1029/2005JE002671|10.1029/2005JE002672.

Glotch, T., and P. Christensen (2005), Geologic and mineralogic mapping of Aram Chaos: Evidence for a water-rich history, *Journal of Geophysical Research-Planets*, 110(E9), doi:10.1029/2004JE002389.

Glotch, T., and A. Rogers (2007), Evidence for aqueous deposition of hematite- and sulfate-rich light-toned layered deposits in Aureum and Iani Chaos, Mars, *Journal of Geophysical Research-Planets*, 112(E6), doi:10.1029/2006JE002863.

Grotzinger, J., et al. (2014), A Habitable Fluvio-Lacustrine Environment at Yellowknife Bay, Gale Crater, Mars, *Science*, *343*(6169), doi:10.1126/science.1242777.

Hamilton, V., and P. Christensen (2000), Determining the modal mineralogy of mafic and ultramafic igneous rocks using thermal emission spectroscopy, *Journal of Geophysical Research-Planets*, *105*(E4), 9717-9733, doi:10.1029/1999JE001113.

Hamilton, V., P. Christensen, and H. McSween (1997), Determining the compositions of Martian meteorites using thermal infrared emission spectroscopy: A precursor to Martian surface spectroscopy., *Meteoritics & Planetary Science*, *32*(4), A55-A55.

Hardgrove, C. J. and A. D. Rogers, Thermal Infrared and Raman Microspectroscopy of Moganite-bearing Rocks, *American Mineralogist*, 98, 78-84, 2013.

Hardgrove C. Rogers A. D, (2014). Natural Micron-Scale Roughness of Chemical Sedimentary Rocks and Effects on Thermal Infrared Spectra. *Eighth International Conference on Mars* [#1392]

Haskin, L., A. Wang, K. Rockow, B. Jolliff, R. Korotev, and K. Viskupic (1997), Raman spectroscopy for mineral identification and quantification for in situ planetary surface analysis: A point count method, *Journal of Geophysical Research-Planets*, *102*(E8), 19293-19306, doi:10.1029/97JE01694.

Hecker, C., M. van der Meijde, and F. van der Meer (2010), Thermal infrared spectroscopy on feldspars - Successes, limitations and their implications for remote sensing, *Earth-Science Reviews*, *103*(1-2), 60-70, doi:10.1016/j.earscirev.2010.07.005.

Kieffer, H. H., and A. P. Zent (1992), Quasi-periodic climatic change on Mars, in *Mars*, edited by H.H. Kieffer et al., pp. 1180-1218, University of Arizona Press, Tucson.

Koeppen, W.C., and V.E. Hamilton (2008). Global distribution, compositions, and abundances of olivine on the surface of Mars from thermal infrared data. *Journal of Geophysical Research-Planets.*, 113, E05001, doi: 10.1029/2007JE002984.

Kraft, M., J. Michalski, and T. Sharp (2003), Effects of pure silica coatings on thermal emission spectra of basaltic rocks: Considerations for Martian surface mineralogy, *Geophysical Research Letters*, *30*(24), doi:10.1029/2003GL018848.

Lane, M., and P. Christensen (1997), Thermal infrared emission spectroscopy of anhydrous carbonates, *Journal of Geophysical Research-Planets*, *102*(E11), 25581-25592, doi:10.1029/97JE02046.

Ling, Z., A. Wang, and B. L. Jolliff (2011a), A systematic spectroscopic study of four Apollo lunar soils, *Journal of Earth Science*, *22*(5), 578-585, doi:10.1007/s12583-011-0208-3.

Ling, Z. C., A. Wang, and B. L. Jolliff (2011b), Mineralogy and geochemistry of four lunar soils by laser-Raman study, *Icarus*, *211*(1), 101-113, doi:10.1016/j.icarus.2010.08.020.

Malin, M. C., and K. S. Edgett (2000), Sedimentary rocks of early Mars, *Science*, *290*(5498), 1927-1937, doi:10.1126/science.290.5498.1927.

Mathew, G., A. Nair, T. Rao, and K. Pande (2009), Laboratory technique for quantitative thermal emissivity measurements of geological samples, *Journal of Earth System Science*, *118*(4), 391-404.

McDaniel, D., S. Hemming, S.M McLennan, G. Hanson (1994), Resetting of neodymium isotopes and redistribution of REEs during sedimentary processes: the early Proterozoic Chelmsford formation, Sudbury basin, Ontario, Canada, *Geochimica Et Cosmochimica Acta*, *58*(2), 931-941, doi:10.1016/0016-7037(94)90516-9.

McLennan, S., et al. (2014), Elemental Geochemistry of Sedimentary Rocks at Yellowknife Bay, Gale Crater, Mars, *Science*, *343*(6169), doi:10.1126/science.1244734.

McLennan, S.M., B. Fryer, and G. Young (1979), Rare-earth elements in Huronian (lower proterozoic) sedimentary rocks: composition and evolution of the post-kenoran upper crust, *Geochimica Et Cosmochimica Acta*, *43*(3), 375-388, doi:10.1016/0016-7037(79)90202-3.

McLennan, S. M. (2012), Geochemistry of Sedimentary Processes on Mars, *Society for Sedimentary Geology*, *102*, 119-138, doi:978-1-56576-313-5.

McLennan, S. M., S. Hemming, D. K. McDaniel, and G. N. Hanson (1993), Geochemical approaches to sedimentation, provenance, and tectonics, *Geological Society of America Special Papers*, *284*, 21-40.

Michalski, J., M. Kraft, T. Diedrich, T. Sharp, and P. Christensen (2003), Thermal emission spectroscopy of the silica polymorphs and considerations for remote sensing of Mars, *Geophysical Research Letters*, *30*(19), doi:10.1029/2003GL018354.

Michalski, J., M. Kraft, T. Sharp, L. Williams, and P. Christensen (2006), Emission spectroscopy of clay minerals and evidence for poorly crystalline aluminosilicates on Mars from Thermal Emission Spectrometer data, *Journal of Geophysical Research-Planets*, *111*(E3), doi:10.1029/2005JE002438.

Michalski, J., S. Reynolds, T. Sharp, and P. Christensen (2004), Thermal infrared analysis of weathered granitic rock compositions in the Sacaton Mountains, Arizona: Implications for petrologic classifications from thermal infrared remote-sensing data, *Journal of Geophysical Research-Planets*, *109*(E3), doi:10.1029/2003JE002197.

Milam, K., H. McSween, and P. Christensen (2007), Plagioclase compositions derived from thermal emission spectra of compositionally complex mixtures: Implications for Martian feldspar mineralogy, *Journal of Geophysical Research-Planets*, *112*(E10), doi:10.1029/2006JE002880.

Moore, D. M., and R. C. Reynolds Jr (1997), *X-ray diffraction and the identification and analysis of clay minerals*, Oxford University Press, New York.

Morris, R., et al. (2010), Identification of Carbonate-Rich Outcrops on Mars by the Spirit Rover, *Science*, *329*(5990), 421-424, doi:10.1126/science.1189667.

Murchie, S., et al. (2009), Compact Reconnaissance Imaging Spectrometer for Mars investigation and data set from the Mars Reconnaissance Orbiter's primary science phase, *Journal of Geophysical Research-Planets*, *114*, doi:10.1029/2009JE003344.

Nesbitt, H. W., and G. M. Young (1996), Petrogenesis of sediments in the absence of chemical weathering: Effects of abrasion and sorting on bulk composition and mineralogy, *Sedimentology*, *43*(2), 341-358, doi:10.1046/j.1365-3091.1996.d01-12.x.

Pettijohn, F. J. (1954), Classification of sandstones, *The Journal of Geology*, *62*, 360-365.

Pettijohn, F. J. (1975), *Sedimentary Rocks*, 3rd ed., Harper & Row, New York.

Ramsey, M., and P. Christensen (1998), Mineral abundance determination: Quantitative deconvolution of thermal emission spectra, *Journal of Geophysical Research-Solid Earth*, *103*(B1), 577-596, doi:10.1029/97JB02784.

Richards, J. A., and X. Jia (2006), *Remote Sensing Digital Image Analysis, An Introduction*, 4th ed., Springer, Berlin, Germany.

Rietveld, H. (1969), A profile refinement method for nuclear and magnetic structures, *Journal of Applied Crystallography*, *2*, 65-71, doi:10.1107/S0021889869006558.

Rogers, A., and O. Aharonson (2008), Mineralogical composition of sands in Meridiani Planum determined from Mars Exploration Rover data and comparison to orbital measurements, *Journal of Geophysical Research-Planets*, *113*(E6), doi:10.1029/2007JE002995.

Ruff, S., P. Christensen, P. Barbera, and D. Anderson (1997), Quantitative thermal emission spectroscopy of minerals: A laboratory technique for measurement and calibration, *Journal of Geophysical Research-Solid Earth*, *102*(B7), 14899-14913, doi:10.1029/97JB00593.

Ruff, S., P. Christensen, D. Blaney, W. Farrand, J. Johnson, J. Michalski, J. Moersch, S. Wright, and S. Squyres (2006), The rocks of Gusev Crater as viewed by the Mini-TES instrument, *Journal of Geophysical Research-Planets*, *111*(E12), doi:10.1029/2006JE002747.

Ruff, S., P. Christensen, D. Blaney, W. Farrand, J. Johnson, J. Michalski, J. Moersch, S. Wright, and S. Squyres (2007), The rocks of gusev crater as viewed by the mini-TES instrument (vol 111, art no E12S18, 2006), *Journal of Geophysical Research-Planets*, *112*(E2), doi:10.1029/2007JE002891.

Ruff, S., P. Niles, F. Alfano, and A. Clarke (2014), Evidence for a Noachian-aged ephemeral lake in Gusev crater, Mars, *Geology*, *42*(4), 359-362, doi:10.1130/G35508.1.

Salisbury, J. W., and L. S. Walter (1989), Thermal Infrared (2.5-13.5μm) Spectroscopic Remote Sensing of Igneous Rock Types on Particulate Planetary Surfaces, *Journal of Geophysical Research*, *94*(NO. B7), 9192-9202.

Squyres, S., et al. (2006), Rocks of the Columbia Hills, *Journal of Geophysical Research-Planets*, *111*(E2), doi:10.1029/2005JE002562.

Squyres, S., et al. (2004), In situ evidence for an ancient aqueous environment at Meridiani Planum, Mars, *Science*, *306*(5702), 1709-1714, doi:10.1126/science.1104559.

Srodon, J., V. Drits, D. McCarty, J. Hsieh, and D. Eberl (2001), Quantitative X-ray diffraction analysis of clay-bearing rocks from random preparations, *Clays and Clay Minerals*, *49*(6), 514-528, doi:10.1346/CCMN.2001.0490604.

Thomson, J. and J. Salisbury (1993), The midinfrared reflectance of mineral mixtures (7-14 μm), *Remote Sensing of Environment*, *45*(1), 1-13, doi:10.1016/0034-4257(93)90077-B.

Tosca, N., D. Johnston, A. Mushegian, D. Rothman, R. Summons, and A. Knoll (2010), Clay mineralogy, organic carbon burial, and redox evolution in Proterozoic oceans, *Geochimica Et Cosmochimica Acta*, *74*(5), 1579-1592, doi:10.1016/j.gca.2009.12.001.

Ufer, K., G. Roth, R. Kleeberg, H. Stanjek, R. Dohrmann, and J. Bergmann (2004), Description of X-ray powder pattern of turbostratically disordered layer structures with a Rietveld compatible approach, *Zeitschrift Fur Kristallographie*, *219*(9), 519-527, doi:10.1524/zkri.219.9.519.44039.

Van der Plas, D., and Tobi, A.C., (1965), A chart for judging reliability of point counting results, *American Journal of Science*, v.264 (1), 87-90.

Vaniman, D., et al. (2014), Mineralogy of a Mudstone at Yellowknife Bay, Gale Crater, Mars, *Science*, *343*(6169), doi:10.1126/science.1243480.

Wang, A., K. Kuebler, B. Jolliff, and L. Haskin (2004), Mineralogy of a Martian meteorite as determined by Raman spectroscopy, *Journal of Raman Spectroscopy*, *35*(6), 504-514, doi:10.1002/jrs.1175.

Wang, A. L., B. L. Jolliff, and L. A. Haskin (1999), Raman spectroscopic characterization of a highly weathered basalt: Igneous mineralogy, alteration products, and a microorganism, *Journal of Geophysical Research-Planets*, *104*(E11), 27067-27077, doi:10.1029/1999je001071.

Ward, C., J. Taylor, and D. Cohen (1999), Quantitative mineralogy of sandstones by X-ray diffractometry and normative analysis, *Journal of Sedimentary Research*, *69*(5), 1050-1062.

Weltje, G., and H. von Eynatten (2004), Quantitative provenance analysis of sediments: review and outlook, *Sedimentary Geology*, *171*(1-4), 1-11, doi:10.1016/j.sedgeo.2004.05.007.

Williams, H., F. J. Turner, and C. G. Gilbert (1954), *PetrographyAn introduction to the study of rock in thin sections* W.H. Freeman and Company, San Francisco.

Wyatt, M., V. Hamilton, H. McSween, P. Christensen, and L. Taylor (2001), Analysis of terrestrial and Martian volcanic compositions using thermal emission spectroscopy: 1. Determination of mineralogy, chemistry, and classification strategies, *Journal of Geophysical Research-Planets*, *106*(E7), 14711-14732, doi:10.1029/2000JE001356.